2. Investigated Processes and Interfaces

This chapter describes the processes of electron transfer and solvation dynamics at adsorbate-metal interfaces and gives an overview of the standard of knowledge in these fields. The first section presents a discussion of the apparently contrary, but actually complementary, theoretical approaches explaining charge transfer at interfaces: Marcus Theory and the tunneling picture. As the investigated adsorbates, ice and ammonia, are polar solvents, section 2.2 gives an overview of electron solvation in polar environments. The investigation of electron solvation phenomena at interfaces offers the additional opportunity to study charge transfer processes. It is shown in section 2.3 that the solvated electron is a model system for the investigation of charge transfer processes at interfaces, as its subsequently changing degree of confinement facilitates the study of electron transfer as a function of coupling strength. Finally, the investigated substrates and adsorbates are discussed: First, a characterization of the adsorbate's properties – of the bare NH_3 and D_2O molecules and their respective condensed phases – is given. Second, the two employed substrates, Cu(111) and Ru(001), are discussed on the basis of their electronic surface band structures. The similarities and differences of these two substrates concerning water and ammonia adsorption are presented in section 2.4.3.

2.1 Electron Transfer

Electron transfer (ET) processes play an important role in a variety of different fields of physics, chemistry, and biology, because many chemical reactions are governed by charge transfer. [Rot90, Tim90, Vog90] In particular, *heterogeneous* electron transfer (HET) at solid-molecular interfaces is of great importance, as such charge transfer processes occur in technologically highly relevant fields, as for example dye-sensitized solar cells or nanoscale electronic devices. [Ada03, Nit03, Zhu04] In addition, the field of electrochemistry and also many surface catalytic processes involve HET. [Mil95, Gad95]

This variety of applications has led to different well-established theoretical approaches describing charge transfer processes. In principle, these different pictures of ET can be discriminated according to discipline: While the physicists, among them Lew D. Landau, mainly focused on charge transfer mediated by wave function overlap and tunneling processes, a chemist, Rudolph A. Marcus, derived a theory for charge transfer processes between two discrete molecular states that are in a solution. An overview of these two approaches to ET is

given in the sections 2.1.1 and 2.1.2. Attempts to merge these seemingly different pictures for charge transfer have also been made in the past. Section 2.1.3 discusses the concept of Truhlar and coworkers, who take into account both, the electron and the solvation coordinate.

2.1.1 Tunneling and Wave Function Overlap

Electron transfer at interfaces, i.e. heterogeneous electron transfer, is often described in terms of wave function overlap with the substrate. Fig. 2.01a illustrates the image potential[2] of an interfacial electron and the corresponding wave function that decays exponentially into the solid. The electron has a non-vanishing residence probability inside the substrate due to its finite wave function overlap. Therefore, the charge transfer time τ_{CT}, i.e. the decay time of the excited state back to the substrate, is strongly determined by the degree of overlap *and* the substrate's electronic properties. [Ech04] Due to the strong influence of surface electronic band structure and density of states (DOS) of the substrate, this picture of charge transfer is termed *substrate-dominated* in the following. It is often used to describe the back relaxation of excited interfacial electrons that are delocalized parallel to the surface plane, such as image potential states (IPS). They form in front of metal surfaces exhibiting an orientational band gap (cf. 2.4.2).[3]

Fig. 2.01b shows another picture for charge transfer from an excited interfacial electronic state to a substrate. It is used to describe the back relaxation of electrons, which are only weakly coupled to substrate states as, for example, excited molecular orbitals. [Bor01] The significantly reduced wave function overlap with the metal states is explained by a tunneling barrier at the interface, which screens the electron from the substrate. [Gad95] As the wave function overlap is significantly reduced, the tunneling probability becomes the rate-limiting step for charge transfer. In other words, τ_{CT} is determined by this tunneling probability only, and the substrate's electronic properties play a minor role in contrast to the substrate-dominated transfer regime. Hence, this picture of HET is termed *barrier-determined* charge transfer in the following.

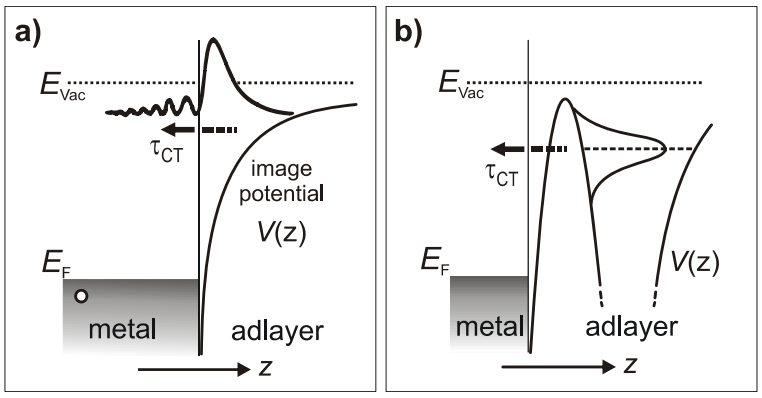

Fig. 2.01: *Two Limits of Electron Transfer at Interfaces.* a) Substrate-dominated charge transfer: The adsorbate-modified and delocalized image potenial state exhibits a finite wave function overlap with the metal. Hence, the direct coupling determines the transfer time τ_{CT}. b) Barrier-determined charge transfer: The transfer time of an electron from a molecular orbital to the substrate is determined by the tunneling probability through the interfacial barrier.

[2] Details on image potential states are discussed in paragraph 2.4.2.

[3] In the case of adsorbate-covered metal surfaces the image potential is modified, as the dielectric constant differs from unity. This affects transfer times and binding energies of the IPS. [McN97, Mar97]

In the past, electron transfer phenomena have been described by either the *substrate-dominated* or *barrier-determined* transfer approach, separately. In the present work it is shown that a transition between these two regimes can occur at molecule-metal interfaces: The solvated electrons investigated here change their degree of confinement with ongoing solvation. Being delocalized right after photoinjection their lateral distribution Δx decreases due to the subsequent screening of the solvent molecules. This evolution of the solvated electron's wave function is accompanied by the formation and further development of the tunneling barrier (cf. 4.1.1). Hence, a dynamic transition between the substrate-dominated and the barrier-determined charge transfer regime is observed.

As excited electronic interfacial states occur typically several eV above the metal Fermi Level E_F, the decay mechanisms of these electrons must also be considered. The transfer of an excited electron to a metal substrate occurs either elastically, i.e. its energy is conserved, or inelastically, i.e. energy is lost to a scattering partner. However, as soon as the excited ("hot") electron is transferred to the metal it relaxes down to the Fermi Level by inelastic scattering processes with other electrons or phonons. This thermalization occurs in metals on femtosecond timescales and has been investigated intensively during the last years. [Fan92, Ret02, Lis04] Fig. 2.02 sketches the electron relaxation due to electron-electron (left) and electron-phonon scattering (right). The excited (blue) electron scatters inelastically (dotted line) with an electron below the Fermi Level (green). Due to the energy exchange ΔE between the scattering partners, an electron-hole pair is generated at the Fermi Level and the excited electron relaxes by ΔE. In the case of electron phonon scattering the phonon energy $\hbar\omega$ increases by the energy loss ΔE of the hot electron (right panel). As electron-phonon scattering processes allow energy transfers of a few 10 meV only, the dominating process for electron relaxation is the electron-electron scattering.

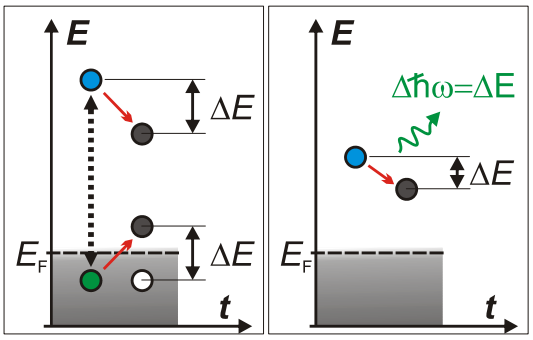

Fig. 2.02: *Scattering Processes in Metals.* Left: Electron-electron scattering. Right: Electron-phonon scattering.

However, before this inelastic relaxation occurs in the metal, the electron has to transfer to the substrate. As mentioned above, this transfer is either mediated by elastic or by inelastic scattering. Fig. 2.03a summarizes these decay mechanisms. At a fixed energy E an electron "senses" unoccupied states in the metal (grey shaded area). Because many single-crystal metal surfaces exhibit an orientational sp-band gap around the center of the surface Brioullin zone (at $k_{\parallel}=0$, see for example Fig. 2.03b), no unoccupied states are available for the back transfer of the interfacial electron within $\pm\Delta k_{gap}$. Hence, in the case of elastic electron transfer, the electron must change its parallel momentum to reach unoccupied states in the substrate. If the back transfer is mediated by inelastic scattering, the electron looses enough energy ΔE to decay to unoccupied metal states below the band gap. As indicated by the arrows in the right panel of

Fig. 2.03b, the energy transferred needs to be larger than the energy difference to the band gap bottom (red arrow) or the electron also changes its momentum upon scattering (green arrow).

In how far the decay probability of an excited electronic state is dominated by elastic or inelastic contributions, depends strongly on the respective substrate. For example in the case of the first antibonding state of a Cs atom adsorbed on copper surfaces, different decay times were observed in experiments on the Cu(111) and the Cu(001) surface. [Oga99, Bau99] This effect was also investigated theoretically in a recent article by Borisov et al. [Bor01] As depicted in Fig. 2.03b the Cu(111) surface exhibits a broader band gap than the Cu(001) surface. The authors calculated the wave packet propagation of the excited Cs state to the respective substrate as depicted in Fig. 2.03c. The electron density is very high at the adatom (below the red dashed line) and comparable for both substrates. However, the wave packet propagation in the metals differs significantly. In the case of Cu(111) (left panel) the density is very high in the normal direction to the surface plane. However, for Cu(001) (right panel) the electron propagates dominantly at an angle to the substrate, i.e. the electron momentum changes. Due to the wider band gap in the case of Cu(111) (cf. Fig. 2.03b) the excited electron decays mainly via inelastic electron-electron scattering to the center of the surface Brioullin zone, without significant momentum change. In the case of

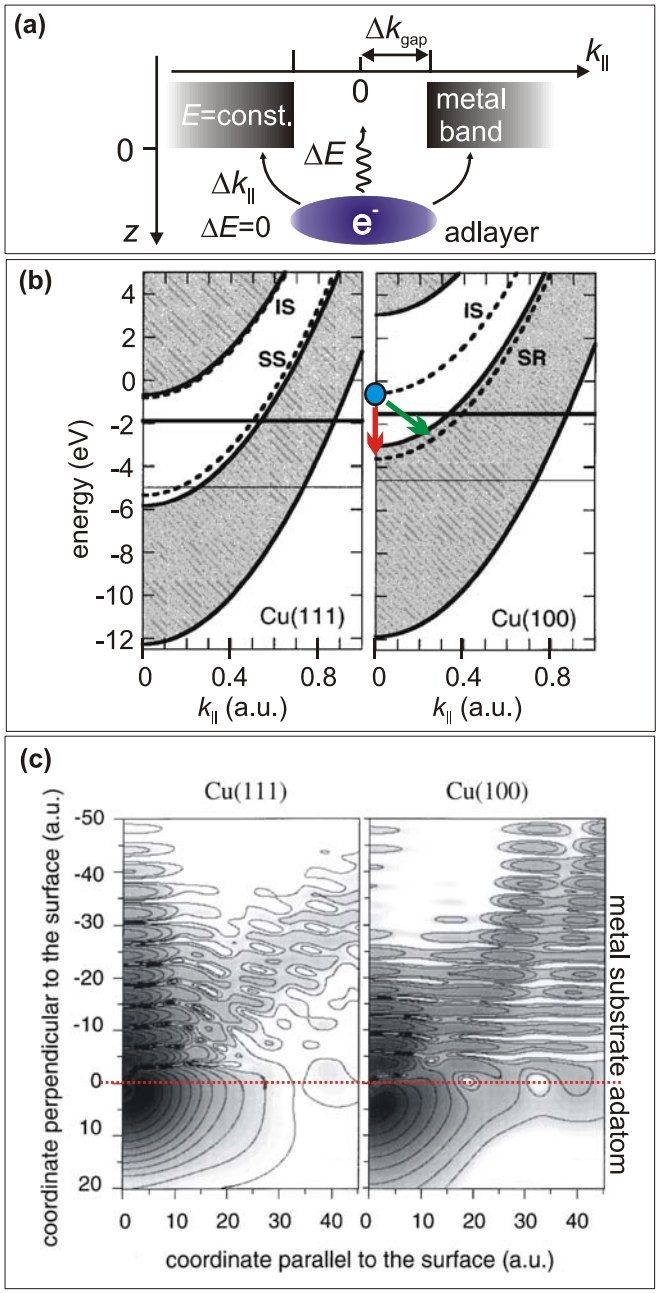

Fig. 2.03: *Relaxation Processes of an Interfacial Electron.* a) Elastic and inelastic relaxation. In the case of inelastic scattering the electron momentum must change by $\Delta k_\parallel$ if an orientational band gap is present. b) Surface electronic band structures of Cu(111) and Cu(001). Note the differing band gap width in *k*-space. c) Wave packet propagation for an excess electron in the first excited state of Cs/Cu(111) and Cu(001). The differing distribution in *k*-space is due to the different band gap widths. (b) and c) adopted from [Bor01])

Cu(001) electron tunneling (accompanied by a momentum change) is the dominating transfer mechanism for the Cs/Cu(001) interface. [Bor01]

The charge transfer of an excited interfacial electron therefore strongly depends on the surface electronic band structure of the underlying substrate if the wave function overlap, and therefore the coupling, is sufficiently strong. If, on the other hand, the electron is efficiently screened from the metal, charge transfer is determined by tunneling through an interfacial barrier that reduces the coupling to the substrate states.

2.1.2 Marcus Theory

Originally, Marcus developed his charge transfer theory for *homogeneous* transfer within a solvent, i.e. for the ET from one distinct molecular state to another. [Mar56, Mar57a, Mar57b] The main challenge was the finding of a manageable description for this multidimensional problem of donor, acceptor, and the abundance of solvent molecules, each having three translational degrees of freedom. In his classical theory, Marcus assumed that the motions of the solvent molecules occur within linear response limits, i.e. the displacements are so small that the assumption of a harmonic intermolecular potential approves correct. [Mar64] The infinite number of possible solvent configurations leads to an enormously complex potential energy surface. Fig. 2.04a shows one slice through this energy landscape, assuming a fixed distance of donor and acceptor, as a function of the collective solvent coordinate q. This coordinate defines changes in the molecular configuration of the solvent. Parabolic potentials for the donor and the acceptor with minima at q_D and q_A result, which correspond to the fully

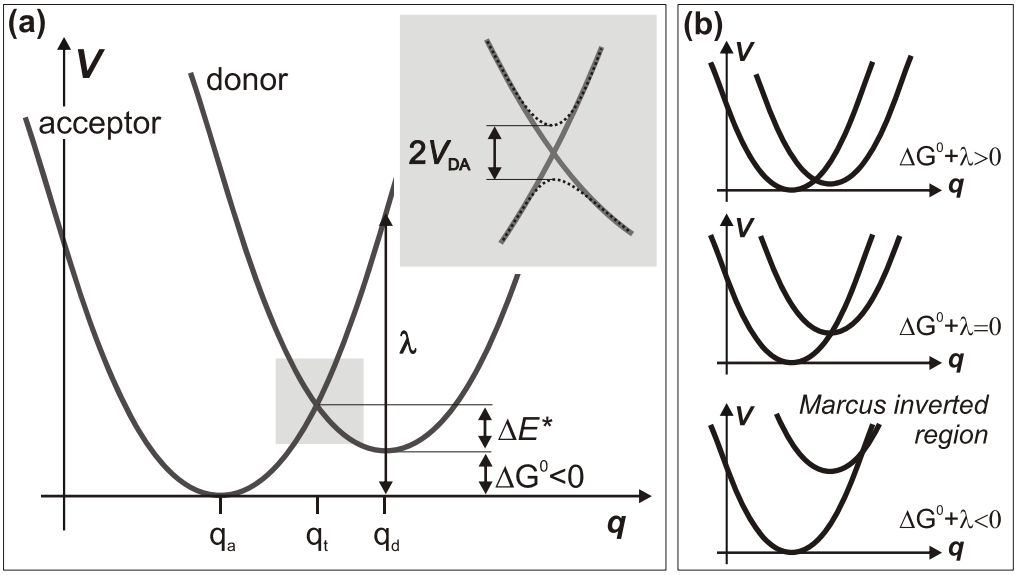

Fig. 2.04: *Marcus Picture for Homogeneous Charge Transfer.* a) Potential energy of the system in the donor and the acceptor state as a function of the collective solvent coordinate q. Inset: The level crossing is avoided depending on the coupling strength between states. b) The transfer rate depends on the energy difference between donor and acceptor level, ΔG^0.

equilibrated species. Fluctuations of the bath bring the donor and acceptor level in resonance at q_t; this transition state region is often termed the *adiabatic crossing point*. Depending on the coupling strength V_{DA} between the two states, an avoided crossing of the potential occurs (cf. inset of Fig. 2.04a). In the *strong coupling limit* charge transfer occurs adiabatically: If the system passes the "intersection" by fluctuation, it will remain at the lowest potential. If there were *no* coupling between the levels, charge transfer would not occur at all. Considering very *weak coupling* between donor and acceptor, fluctuations across q_t would make the system "jump" to the upper surface and back; [Mar60] in this case ET occurs with the probability

$$k_{\text{homo}} = \frac{2\pi}{\hbar} \cdot \langle V_{DA} \rangle^2 \cdot FC, \tag{2.1}$$

where FC is a thermally averaged Franck-Condon factor that describes the influence of temperature on the charge transfer rate by a Boltzmann distribution of the vibronic levels in the harmonic (parabolic) potential:

$$FC \propto \exp\left(-\frac{\Delta E^*}{k_B T}\right) \qquad \text{(Boltzmann factor } k_B\text{, temperature } T\text{)} \tag{2.2}$$

The activation energy ΔE^* for charge transfer is the energy difference between the potential minimum and the intersection of donor and acceptor parabola as depicted in Fig. 2.04a. Hence, the resulting transfer rate (2.1) describes the transfer from a donor in thermal equilibrium. As easily derived analytically, ΔE^* depends on the reorganization energy $\lambda > 0$, which is required to distort the solvent from q_d to q_a, and on the available free energy of the reaction, $\Delta G^0 < 0$:

$$\Delta E^* = \frac{\left(\lambda + \Delta G^0\right)^2}{4\lambda} \qquad \text{[Mil95]} \tag{2.3}$$

The electron transfer rate (2.1) hence becomes a Gaussian as a function of ΔG^0

$$k_{\text{homo}} = \frac{2\pi}{\hbar} \cdot \langle V_{DA} \rangle^2 \cdot \left(\frac{1}{4\pi|\lambda|k_B T}\right)^{\frac{1}{2}} \cdot \exp\left(-\frac{\left(\lambda + \Delta G^0\right)^2}{4\lambda k_B T}\right), \tag{2.4}$$

which is the famous Marcus curve. As sketched in Fig. 2.04b the transfer rate increases with increasing $|\Delta G^0|$ and reaches its maximum when $\Delta G^0 + \lambda = 0$, i.e. when the absolute value of the free energy of the reaction $|\Delta G^0|$ equals the reorganization energy λ. This happens when the acceptor parabola intersects the donor potential at its minimum; the maximum of k_{homo} can be intuitively understood (cf. Fig. 2.04b, center). For $\Delta G^0 + \lambda < 0$ the so-called *Marcus inverted region* is reached; the transfer rate becomes smaller although the free energy difference becomes larger. Note, that k_{homo} does not describe the transfer rate at a certain solvation coordinate q; it takes into account the Boltzmann distribution within the harmonic potential and thus gives the total rate for all q.

Extension of this model to the *heterogeneous* problem, the transfer from a distinct state to a metal (electrode) offering a continuum of unoccupied states above the Fermi Level E_F, requires

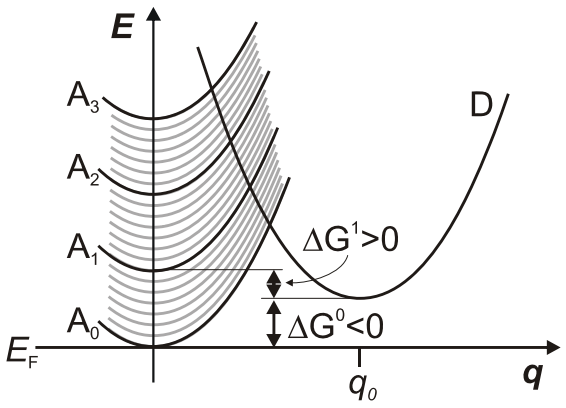

Fig. 2.05: *Marcus Picture for Heterogeneous Charge Transfer.* Due to the continuum of unoccupied states that is offered by the metal electrode, a series of parabolas has to be taken into account, which all intersect the donor level D. The transfer rate to each of them is determined by the respective energy difference between their minima and D(q_0).

a continuum of accepting parabolas as depicted in Fig. 2.05. [Mil95, Zhu04] The energetically lowest level corresponds to the lowest unoccupied states of the metal close to E_F, here denoted as A_0. The transfer rate from the donor state to A_0 exactly follows Eq. (2.4). Transfer to the energetically higher lying states, as for example A_1, requires consideration of the varying energy difference between the respective parabola minima. Fig. 2.05 illustrates that the free energy difference ΔG^i may also become positive. Integration of the resulting rate constants weighted by the Fermi-Dirac distribution $f(E)$ around E_F and the metal's DOS $\rho(E)$ leads to the total rate of HET:

$$k_{\text{hetero}} = \int_{-\infty}^{\infty} \frac{2\pi}{\hbar} \cdot \langle V_{DA} \rangle^2 \cdot (1 - f(E)) \cdot \rho(E) \cdot \left(\frac{1}{4\pi\lambda k_B T} \right)^{\frac{1}{2}} \cdot \exp\left(- \frac{\left(E + (\lambda + \Delta G^0)\right)^2}{4\lambda k_B T} \right) dE \qquad (2.5)$$

For constant coupling V_{DA} and constant density of states $\rho(E)$, this expression can become temperature-independent, because the integral of a Gaussian is always proportional to its width (here $(4\lambda k_B T)^{1/2}$). If $(\lambda+\Delta G^0) < 0$, the donor parabola D is in the inverted region (cf. Fig. 2.04b). This means that D is intersected by acceptor levels A_i down to its minimum and non-activated charge transfer can occur at any $q<q_0$, regardless of the Boltzmann distribution of donor states. In the case of $(\lambda+\Delta G^0) > 0$, i.e. the minimum of D lies below the intersection with A_0, charge transfer is temperature-dependent, because even for ET to A_0, a potential barrier ΔE^* has to be overcome.

For the above described approach of weak electronic coupling it was assumed that the energy of the photoexcited donor state is already distributed over its vibrational levels. [Mil95] This means the process of electron solvation (i.e. equilibration with the solvent) has to occur on a much faster timescale than the electron transfer. Such a Boltzmann distribution is not necessarily reached for excited ("hot") electrons in ice or ammonia layers on metal surfaces, as the transfer occurs here on fs-timescales. For these systems electron transfer and solvation compete with each other and a thermally equilibrated solvated electron distribution around the potential minimum cannot be assumed automatically. Paragraph 4.1.4 discusses, in how far equation (2.5) has to be modified to account for the non-equilibrated hot electrons and whether or not charge transfer is temperature-dependent for the investigated systems.

2.1.3 Truhlar Concept

The potential energy curves discussed in the previous section describe the total energy of the solvent-solute-electrode system as a function of the multidimensional reaction or solvation coordinate *q*. Regardless of whether weak or strong coupling (non-adiabatic or adiabatic charge transfer, respectively) is considered, the actual transfer occurs in the *adiabatic crossing point region* by the transition of the electron from the donor to the acceptor state. As donor and acceptor are spatially separated from each other, this transfer also occurs along the real space coordinate. It is generally accepted [Mil95, Nit01, Sch01, Zhu04] that the underlying process is the tunneling along the real space (electron) coordinate. Schenter, Garrett, and Truhlar were the first to theoretically describe a homogeneous charge transfer process in the presence of a solvent (in their case proton transfer) in a two dimensional manner with the two coordinates for solvent and solute as depicted in Fig. 2.06.[4] Note that the authors use – in contrast to the

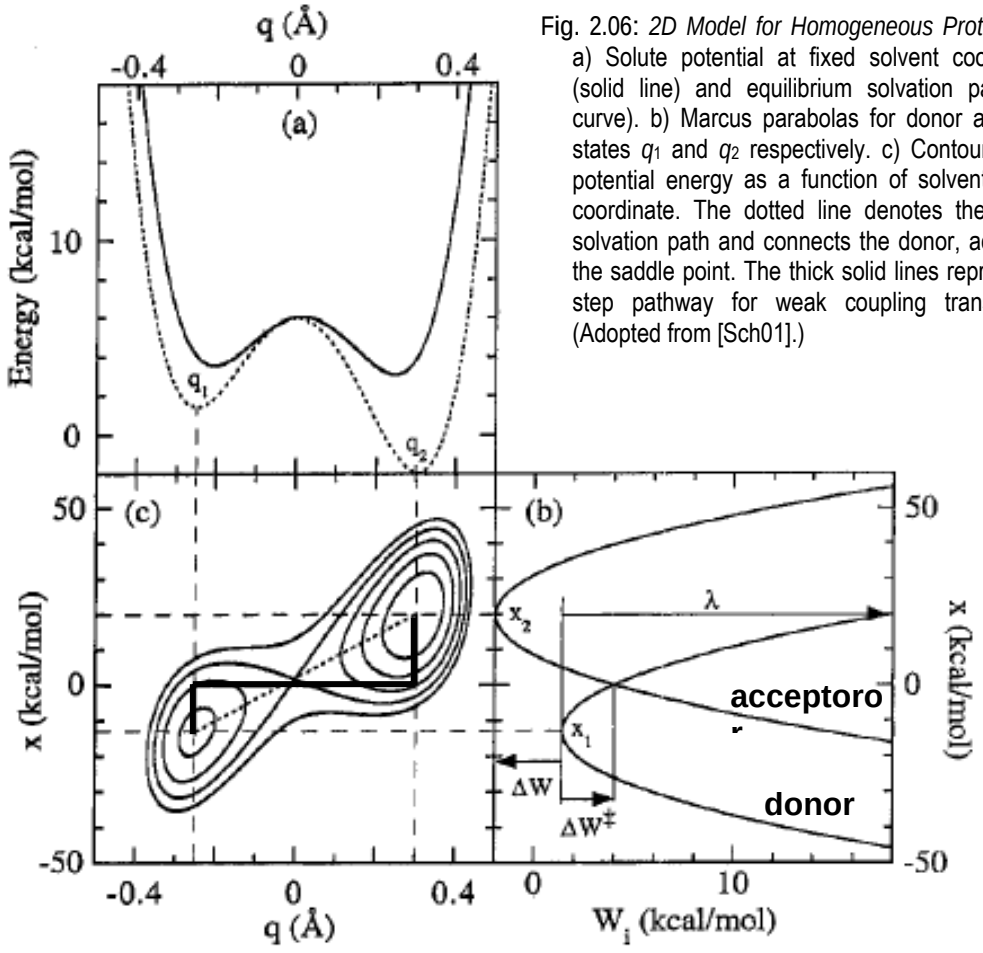

Fig. 2.06: *2D Model for Homogeneous Proton Transfer.* a) Solute potential at fixed solvent coordinate *x*=0 (solid line) and equilibrium solvation path (dashed curve). b) Marcus parabolas for donor and acceptor states q_1 and q_2 respectively. c) Contour plot of the potential energy as a function of solvent and solute coordinate. The dotted line denotes the equilibrium solvation path and connects the donor, acceptor, and the saddle point. The thick solid lines represent the 3-step pathway for weak coupling transfer theory. (Adopted from [Sch01].)

[4] Miller and coworkers also developed a 2D model for proton transfer in 7-azaindole dimers. However, besides the real space proton coordinate they invoked a "symmetric stretch" coordinate to account for the intramolecular degrees of freedom of these large molecules. [Gua99] Although this is not quite the same as the solvent coordinate here, the concept of a 2D-potential, describing proton transfer as a function of *N* >>2 degrees of freedom, is comparable to the Truhlar Model.

nomenclature in this work – the variable q for the solute coordinate (i.e. the real space transfer coordinate of the proton) and x for the solvent coordinate.

The figure shows a contour plot of equal potential energies of the system as a function of the solvent and solute coordinate (Fig. 2.06c). (a) and (b) depict cuts through this 2D surface as a function of q and x, respectively. As indicated by the vertical dashed lines, the potentials given in Fig. 2.06b are slices through the minima of the reactant (donor) and the product (acceptor) state at q_1 and q_2, respectively. These are the Marcus parabolas discussed in the previous paragraph. In the weak coupling limit, charge transfer occurs in three steps: (i) Due to thermal activation the system reaches the intersection of the two parabolas. This corresponds to a change of configuration, i.e. a change of x (with q fixed). (ii) At the crossing the charge tunnels through the potential barrier along the transfer coordinate q (with x fixed). The associated potential is the solid line in Fig. 2.06a. (iii) Transferred to the acceptor Marcus parabola the system relaxes (along x, fixed q) to the minimum. This solvation path is represented in (c) by the three thick solid lines connecting the two minima of donor and acceptor.

The dotted line in Fig. 2.06c represents the equilibrium solvation path, which is achieved by following the steepest gradient of the saddle point at $x = q = 0$. According to Truhlar and coworkers this is not necessarily the path along which the transfer occurs; depending on the solute mass they calculate different minimum energy paths through their 2D potential that deviate from the dotted line. [Sch01]

The main idea of the work described above is – according to the authors – to treat the solvent and solute coordinate "on a nearly equal footing". The weak-overlap theory with its non-equilibrium solvation coordinate has proven to be applicable for a high number of charge transfer reactions in the past, but does not, however, explicitly take into account other coordinates. This approximation is certainly correct when fluctuations of the solvent are the dominant factor influencing the reaction. Yet, "charge transfer theory cannot give reliable results for cation or anion transfer without allowing for the realistic shape of the equilibrium solvation potential and the possible participation of many degrees of freedom." [Sch01]

One important result of Truhlar's work is – besides possibly upcoming new expressions for charge transfer rates and activation energies based on the extended (equilibrium) solvation path – the unification of the real space reaction coordinate with the solvent bath coordinate in a very demonstrative way. It illustrates that charge transfer reactions should not be viewed in a linear manner. Instead, consideration of all contributing factors (tunneling and Marcus coordinates) is required, although their respective influence has to be kept in mind. In the authors' words, the Truhlar Concept "should be especially useful for understanding the crossover between bath-controlled dynamics and solvent-independent vibrationally controlled dynamics".

Having introduced three pictures of charge transfer, the Landauer, Marcus, and Truhlar approach, it may be concluded that these concepts are not contradictory, but highly complementary. However, depending on the system investigated one or the other theory might be more appropriate to highlight the dominating charge transfer mechanism: Real space or bath coordinate *or* the interplay between them. The electron transfer dynamics investigated in the

present work occur at water- and ammonia-metal interfaces. Therefore, the next section summarizes the standard of knowledge of electron solvation in liquid NH_3 or water and in ice and NH_3 gas phase clusters.

2.2 Electron Solvation

The injection of an excess electron into a polar environment such as water or ammonia leads to a reorientation of the surrounding molecules, because their dipole moments react to the electric field of the additional charge.[5] The resulting energetic stabilization (gain in binding energy) of the electron is called *electron solvation* and – depending on the solvent – also often termed *electron hydration* or *ammoniation*. The first observation related to solvated electrons was made almost 200 years ago by Humphry Davy, who reported a blue color of ammonia containing compounds. [Dav08] In 1908, this effect was attributed to the absorption of excess electrons, which are surrounded by a cavity of NH_3 molecules. [Kra08] Electron hydration was first discovered by Hart and Boag in 1962 [Har62] leading to an avalanche of studies in a variety of different fields, in which solvated electrons play a role, ranging from electrochemistry [San98] to the enhanced dissociation of CFCs (*chlorofluorocarbons*) in stratospheric clouds [Lu99, Lu01 and references therein].

Solvated Electrons in Liquids: It is important to distinguish between three different procedures of generating excess electrons in a liquid solvent:

(i) Charge Transfer from an admixed atom/molecule (e.g. alkalis) or ion (e.g. halides) via so-called CTTS (*charge transfer to solvent*) states. The presence of the parent ion or atom, however, may lead to a modification of the electron solvation dynamics. [Tho03]

(ii) Charge separation from the solvent molecules after photoexcitation of the molecules. This requires either high photon energies or multi-photon processes, because liquid water and ammonia are both insulators, exhibiting a wide band gap (8 eV for water [Guo02] and 20 eV for NH_3 [Pea92]). Here, the solvated electron's lifetime is determined by the recombination probability with the parent ion. [Tro88, Son01]

(iii) Capture of low-energy electrons after irradiation. This procedure contains the risk of electron-induced dissociation due to dissociative electron attachment. [Han90]

After generation of excess electrons of any kind, both, liquid water and ammonia exhibit characteristic optical absorption signatures. These result from an optical transition of the solvated electron (s-like) ground state into excited states below the conduction band (CB) minimum. As depicted in Fig. 2.07 the absorption maximum lies at ~1.7 eV for water and therefore considerably higher in energy than for ammonia (~0.8 eV). However, the optical absorption depends strongly on temperature; for water, the absorption maximum shifts with a rate of 2.5 eV/K to lower photon energies with increasing temperature. [Jou79] In both cases

[5] Electron solvation is also known in non-polar solvents with a high polarizability. [Lad96]

the spectra are asymmetric, with a long tail to higher photon energies, and are quite broad.[6] This spectral shape does not change over a wide range of temperatures.

Electronic transitions and molecular reorientations occur on femto- and picosecond timescales. Hence, ultrafast time-resolved techniques employing femtosecond laser pulses are a powerful tool to investigate the s-to-p transition in liquid water and ammonia. Using time-resolved optical absorption spectroscopy to investigate the early dynamics of the hydrated electron, it was shown that states excited with low photon energies are localized. However, the absorption of photons above 3.1 eV leads to the population of delocalized conduction band (CB) states of liquid water. [Ass99, Son01, Kam02] In addition to this variety of excited states a coupling to vibrational modes of the solvent molecules also comes into play: The ground and excited state potential exhibit different curvatures. The back relaxation to the ground state occurs therefore to vibronically excited levels, which results in a broadening of the spectra. [Bal99, Fri92]

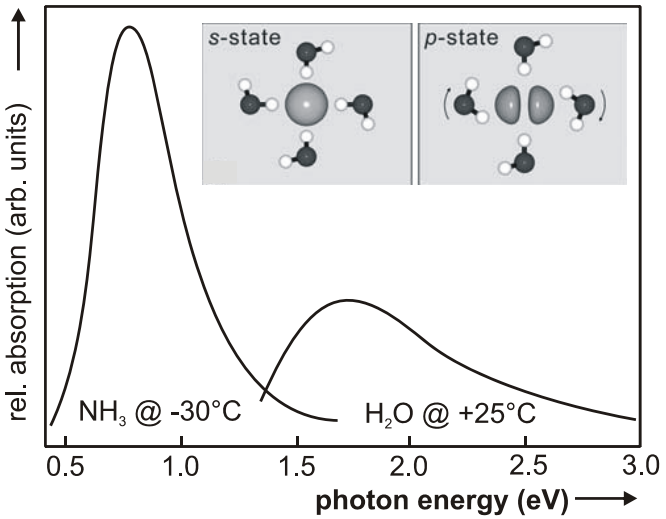

Fig. 2.07: *Optical Absorption Spectra of Liquid Water and Ammonia.* The solvated electron leads to a characteristic optical absorption spectrum due to a transition from its ground state into excited states (based on [Sch68]). Inset: The cavity model of the solvated electron in water attributes these spectral features to an s-to-p transition within a cavity of six water molecules (adopted from [Bal99]).

One frequently used picture for solvated electrons and their local environment is the so-called *cavity model*. It is assumed that the solvated electron is localized in an s-like state in a cavity of 6-8 molecules, which form the first solvation shell (cf. the inset of Fig. 2.07). [Spr94, Bal99, Lin06] Within the so-formed potential three p-like excited states (p_x, p_y, p_z) evolve. Due to deviations from the spherical symmetry of the cavity, these excited states are not degenerate. According to this model, the absorption spectrum is dominated by these s→p transitions. However, some experiments with mixed solvents cannot easily be explained by the cavity model. They suggest that the inner solvation "shell" consists of one or two water molecules. [Mar99] The *solvent anion complex* (SAC) *model* proposes that indeed a small, negatively charged water cluster is solvated instead of the bare electron. [Tut91, Erm02] Another approach is the *multimer radical anion model* suggested for NH_3, which assumes that the solvated electron is delocalized on nitrogen orbitals of the cavity-forming ammonia molecules; the cavity results here due to the repulsion of the negatively charged molecules. [Shk06]

[6] The absorption of the ammoniated electron in the red part of the visible spectrum leads to the blue color of ammonia mentioned above.

During the last decades, the formation dynamics of solvated electrons in liquid water has been investigated intensively using time-resolved absorption spectroscopy after multi-photon ionization of water molecules. [Mig87, Pep97, Ass99, Mad00, Vil01, Her02, Kam02] Many authors suggest the existence of presolvated, "wet" electron states, which are localized, but exhibit different time constants for optical absorption than the ground state. [Mig87, Ass99, Kam02] However, the interpretations of the formation dynamics differ. Performing temperature-dependent studies, Madsen et al. suggest that the spectral shift of the absorption spectrum results from a thermal relaxation of the hydrated electron, because it coincides with the temperature-dependent change of the ground state solvated electron.[7] [Mad00] However, Barbara and coworkers suggest that electron trapping occurs via several prehydrated states including the p-excited state of the solvated electron. The dynamics observed are attributed to a subsequent rearrangement of the solvation shell. [Kam02] Studies on the p-state dynamics support this picture. Using time-resolved photon echo experiments and developing a theoretical wave packet propagation model, Baltuska et al. propose that the dynamics observed result from an unequilibrated solvation shell that has to reorient after p-state excitation. [Bal99]

Electron Solvation in Gas Phase Clusters: In the past few decades much effort has been invested in the study of electron solvation in gas phase water and ammonia anion clusters, including photoelectron spectroscopy experiments. These investigations had two main objectives: (i) Exploration of the number of required solvent molecules to solvate an excess electron and (ii) Gain of further understanding of the properties of the solvated electron in the liquid. Furthermore, the ability to control cluster size and temperature facilitates quantitative comparison of theory and experiment. For both solvents, water [Ver05a] and ammonia [Sar02], a linear dependence of the vertical binding energy (VBE) of the solvated electrons on $n^{-1/3}$ (where n represents the number of molecules in the anion cluster) was found. The extrapolated values for $n \rightarrow \infty$ (i.e. for the liquid) agree quite well with the ones for the sodium-doped liquids of 3.2 eV for water and 1.4-1.6 eV for ammonia. [Häs40, Aul73]

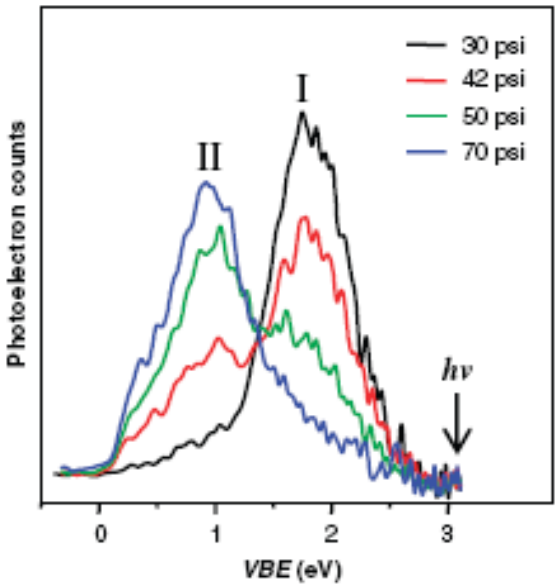

Fig. 2.08: *Photoelectron Spectra of $(D_2O)_{50}^-$ Clusters under Varying Baking Pressures.* Depending on preparation conditions bulk- (I) and surface-bound (II) electrons are observed (adopted from [Ver05a]).

Due to the finite size of the investigated anion clusters the question emerges whether the observed electrons solvate on the surface or in the bulk of the clusters. This issue has been controversially discussed for several years, [Pai04, Ver05a, Tur05a, Ver05b, Tur05b,

[7] Similar conclusions were drawn for the p-state dynamics in liquid ammonia. [Lin06]

Coe06] as several different interpretations of experiments and theory arose. For example, theory predicted bulk-bound electrons for clusters with $n \geq 64$, [Bar88] while experiments found solvated electrons down to $n=11$, who's VBE can be extrapolated to the bulk value as mentioned above. [Coe90, Coe01] That the photoelectron spectra of water anion clusters seem to depend dramatically on the baking pressure of the respective experimental setup, complicates the interpretation considerably: Fig. 2.08 shows photoelectron spectra of $(D_2O)_{50}^-$ clusters for different baking pressures. The peak at 2 eV corresponds to solvated electrons whose size dependence follows the one published in [Coe90]. Those are termed "isomer 1". The second peak at lower energies, isomer II, corresponds according to Verlet et al. to surface bound electrons, as the electrons are less strongly bound than for isomer I. [Ver05a] In addition to these two isomers a third one at even lower VBE and with quite low intensities is observed for $11 \leq n \leq 35$ (not shown here), which the authors assign to another surface-bound state of a more diffusive character than isomer II. This finding was confirmed recently by the photoelectron spectroscopy study of Coe and coworkers. [Coe06] However, with their quantum classical simulations Turi et al. confirm the results of Barnett et al. [Bar88] and claim that *all* experimentally observed features up to now have to be assigned to surface-bound hydrated electrons. [Tur05a]

It can be concluded that – although disagreeing on the size range – experiment and theory find bulk and surface solvated species for the gas phase clusters. As adsorbed molecular layers exhibit, just like the clusters, a finite size (but only in one dimension), a comparison of the solvated electron dynamics suggests itself. Because D_2O can form clusters or islands on the Cu(111) surface (cf. 4.1.2), such a comparison becomes even more promising. Paragraph 4.1.3 shows that the surface science approach employed here facilitates the observation of a surface-to-bulk transition at D_2O coverages corresponding to $n \approx 40$ clusters.

In the previous two sections the physics background of electron transfer and solvation dynamics was presented. As these dynamics occur simultaneously at polar molecule-metal interfaces, the next section presents previous works on this subject, especially focusing on ice-metal interfaces.

2.3 Transfer and Solvation at Interfaces

The solvation dynamics in liquid water and ammonia as well as in gas phase clusters have been investigated by several groups using externally added excess electrons (e.g. electron beams or doping) or photodetached electrons from the solvent molecules as discussed in the previous section. These procedures invoke several side effects as mentioned further above. The investigation of electron solvation dynamics at *interfaces* facilitates another possibility of charge injection: The substrate acts as an electron source, from which electrons are transferred into the adlayer after photoexcitation. The advantage of this procedure is the observation of electron solvation dynamics without the presence of an electron-donating atom or ion, because the hole created in the metal substrate is efficiently screened. Yet, these investigations are challenging to some extend, as the substrate offers a continuum of unoccupied states to which the excited electrons decay via elastic and inelastic scattering processes as discussed in section 2.1. Consequently, the lifetime of an electron in the adlayer is limited by its back transfer probability to the metal or semiconductor, which normally occurs within few picoseconds. [Mil02, Li06]

However, this restriction turns out to be a benefit, as charge transfer processes across interfaces are of fundamental significance in a variety of different fields ranging from classical electrochemistry to nanoscale electronic devices. [Mil95, Zhu04] As discussed in the next paragraph, the solvated electron changes its degree of confinement dynamically after photoinjection. Due to the rearrangement of the surrounding molecules, the coupling of the electronic wave function to substrate states is reduced as time proceeds. Therefore, the solvated electron facilitates the exploration of the competition of charge transfer and solvation in real time and is thus a model system for HET.

In the past, many studies focused on the investigation of the electron transfer and solvation dynamics at various molecule-metal interfaces, including water, alcohol, and alkane layers, and at molecule-semiconductor interfaces. [Ge00, Gah02, Bov03, Szy05, Li06, Zha06a, Zha06b] However, no investigation of electron solvation dynamics in ammonia layers has been published yet. All of the mentioned studies find a transition from a delocalized electronic state to a localized (solvated) state. However, the authors suggest different pathways:

(i) The excess electron localizes via so-called *small polaron formation*, where the electron couples to molecular modes so that a localized state is formed.

(ii) The localization occurs by the transition from a delocalized state into *pre-existing traps* in the adsorbate layer.

The excess electron has to be injected from the substrate into the adsorbate layer before the localized state is formed. The electron solvation dynamics at interfaces therefore actually involve *two* charge transfer processes, the electron transfer from the underlying substrate into

the adlayer *and* the back transfer from the localized solvated electron state to the continuum of unoccupied states in the substrate. The subsequent paragraphs present the results of C. Gahl's dissertation on the electron transfer and solvation dynamics at ice-metal interfaces. [Gah04] They serve as a summary of the state of knowledge at that time and introduce the fundamental steps of charge transfer and solvation at ice-metal interfaces. Performing accurately adjusted data analysis procedures in combination with systematically accustomed new experiments on the same system, the present work achieves a wider understanding of the fundamental processes occuring at these interfaces as shown in chapter 4.

2.3.1 Ultrafast Dynamics in Amorphous Ice on Cu(111)

Fig 2.09 shows the time-resolved two-photon photoelectron (2PPE) spectra of a 4 BL thick amorphous D_2O adlayer on the Cu(111) surface.[8] In the left panel the 2PPE intensity is plotted in false color representation (see scale on the top) as a function of time delay between pump and probe laser pulse (bottom axis) and energy with respect to Fermi and vacuum level (left and right axis, respectively). The right panel depicts 2PPE spectra of the same dataset versus intermediate state energy for a series of different time delays (right axis). The spectra exhibit two features, a broad, short-lived continuum around zero time-delay and a sharp peak below $E - E_F = 3$ eV, which shifts down to lower energies with increasing time delay. It was shown by

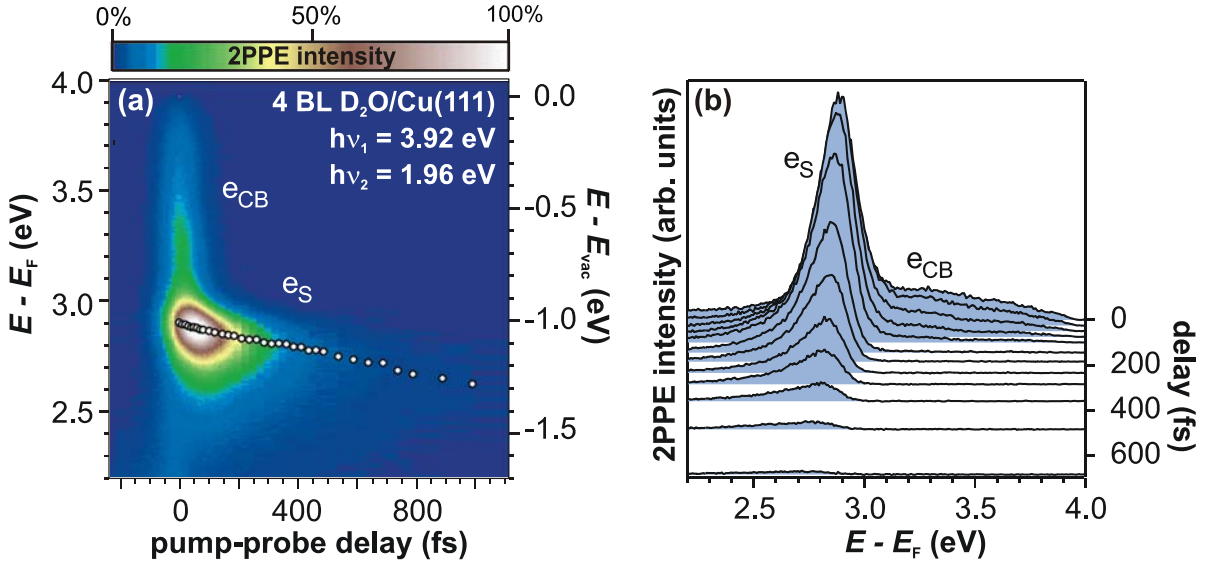

Fig. 2.09: *Time-Resolved 2PPE Spectra of Amorphous D_2O/Cu(111).* (a) 2PPE intensity (false color representation) as a function of pump-probe delay (bottom axis) and energy with respect to E_F (left axis) and E_{vac} (right axis). White circles correspond to the peak maximum of the solvated electron feature e_S. (b) 2PPE spectra of the same measurement as a function of intermediate state energy (bottom axis) at a series of different time delays (right axis). The broad continuum e_{CB} corresponds to the ice conduction band and decays within the laser pulse duration. The long-living feature of the solvated electrons shifts to lower energies with increasing time delay as indicated by the markers in panel (a). (Adopted from [Gah04].)

[8] Details on the coverage determination and 2PPE data acquisition are given in chapter 3.

angle-dependent measurements that the former is delocalized parallel to the surface and that the latter becomes further localized with increasing time delay. [Gah02, Bov03, Gah04] The subsequent degree of confinement, which is governed by the energetic shift of the peak maximum (white circles in Fig. 2.09a), allows the assignment of the peak to solvated electrons (e_S) in the ice adlayer. Due to its delocalized character the broad continuum can be assigned to the ice conduction band (CB). While the conduction band electrons decay within the laser pulse duration, the solvated electrons exhibit a finite lifetime to positive delays: After photoinjection into the adlayer they are localized and stabilized by the surrounding water molecules. The subsequent screening from the Cu(111) substrate leads to a reduction of their decay probability so that the temporal evolution of e_S can be analyzed up to 1 ps. In other words, the stabilization competes with the electron transfer.

Fig. 2.10 summarizes all involved fundamental steps of electron transfer and solvation at the investigated interface: Injection (1), solvation (2), and back transfer (3). The left panel depicts these processes as a function of electron (real space) coordinate z: After photoexcitation of metal electrons from below the Fermi Level into unoccupied metal states the electron is injected into the adlayer via the delocalized conduction band (1). The excess electron localizes in preexisting traps near the bottom of the ice conduction band (dotted circle). Subsequently, it is energetically stabilized by a reorientation of the surrounding polar molecules, i.e. solvated (2). At the same time the solvated electron population decays back to the metal substrate (3). The dynamic evolution of the energetic position of the solvated electrons and the population of the solvated electron state is probed by a second, time-delayed ultrashort laser pulse, which excites

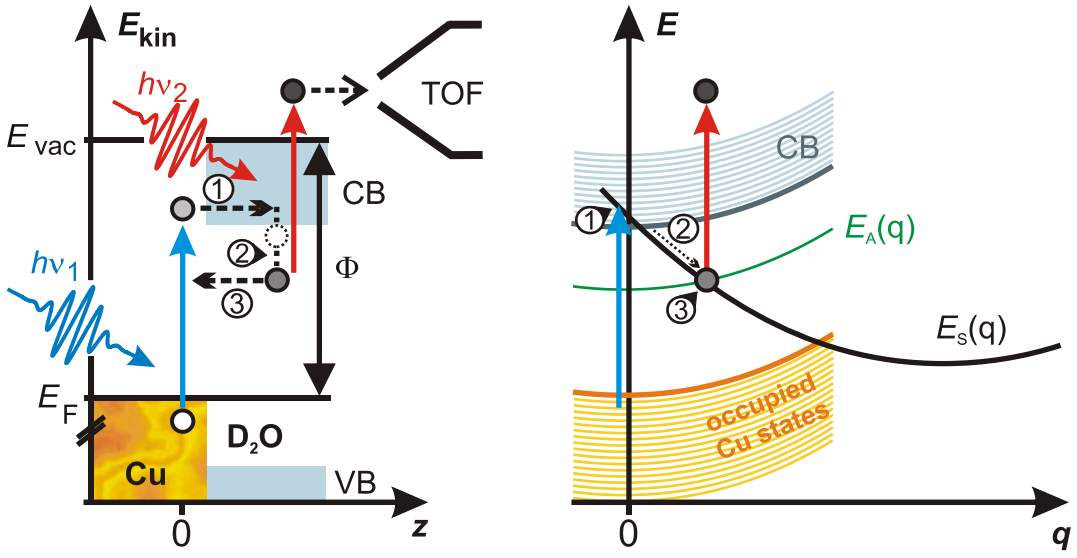

Fig. 2.10: *Fundamental Steps of Electron Transfer and Solvation.* Schematic representation of the fundamental processes involved for charge transfer and solvation at ice-metal interfaces: (1) Injection, (2) solvation, and (3) back transfer of the electron. Left: Course of events as a function of (real space) electron coordinate *z*. Right: Marcus picture for ET and solvation: Total energy potentials for an electron in the ice conduction band (blue), in the solvent (black), and in the metal (orange and green) as a function of solvent coordinate *q*. ET occurs when the parabolas intersect. See text for details.

the remaining electron population above the system's vacuum level so that their kinetic energy can be analyzed by the time of flight spectrometer.

The right panel presents the same course of events as a function of solvent coordinate q that subsumes the solvent (ice) degrees of freedom as introduced in section 2.1.2. The orange parabolas correspond to occupied metal states, from which electrons are excited. The iso-energetic transfer to the ice conduction band (blue parabolas), i.e. electron injection (1), occurs at the intersections of the CB states with $E_S(q)$. As soon as the electron is localized in the ice, the system moves on the solvated electron potential $E_S(q)$ (black curve) to higher q (i.e. stronger lattice distortion). The energy of the solvated electron is reduced due to the rearrangement of the solvent molecules (2). $E_S(q)$ is intersected by parabolas of unoccupied metal states as exemplarily sketched by the green potential $E_A(q)$, which is one exemplary acceptor state. The transfer probability from $E_S(q)$ to $E_A(q)$ (3) is determined by the coupling matrix element between the two levels.

Open Questions: It is apparent from Fig. 2.10 that for a complete description of electron transfer and solvation dynamics at ice-metal interfaces both, electron and solvent coordinates, have to be taken into account, as neither reveals real space and lattice dynamics in an equal fashion. However, to quantitatively interpret the transfer and solvation dynamics at ice-metal interfaces, the substrate influence on the electron dynamics has to be identified (cf. 4.1.1). Also the impact of the ice morphology on the electron dynamics is of high significance for the distinction of electron solvation and transfer processes. This question is addressed in paragraph 4.1.2. The finite size of the adsorbed ice layers allows for the investigation of the solvation site, surface vs. bulk, of the excess electrons, which is still under discussion for the gas phase clusters (cf. 2.2). This issue and the difference between electron dynamics in adsorbed ice layers and in adsorbed ice clusters (not shown here) is discussed in 4.1.3. Finally, the degree of coupling of the solvated electron to the underlying substrate and therefore the applicability of the Landauer and Marcus approach to the problem is explored in paragraph 4.1.4 by temperature-dependent experiments.

2.3.2 Ultraslow Dynamics in Crystalline Ice on Cu(111)

The electron dynamics in crystalline D_2O layers were investigated at the ice-Ru(001) interface. For electron solvation, a striking observation was the occurrence of a solvated electron state, which exhibits remarkable lifetimes of several minutes. The left panel of Fig. 2.11 depicts 2PPE spectra of this ultralong-living state as a function of intermediate state energy with respect to the metal's Fermi Level for a series of different time delays. After 0.1 s the peak lies 2.1 eV above E_F. With increasing time delay the peak intensity decreases as depicted in the upper inset. The time constant of this population decay (exponential fit) adds up to 10 min. Such an enormous lifetime (compared with the femtosecond dynamics shown in 2.3.1) is highly unusual for an excited electron in front of a metal surface: The trapped electron has to be completely screened from the metal, as it would otherwise decay within picoseconds. In addition it is remarkable that this trapped electron state e_T exhibits a shift of its peak maximum

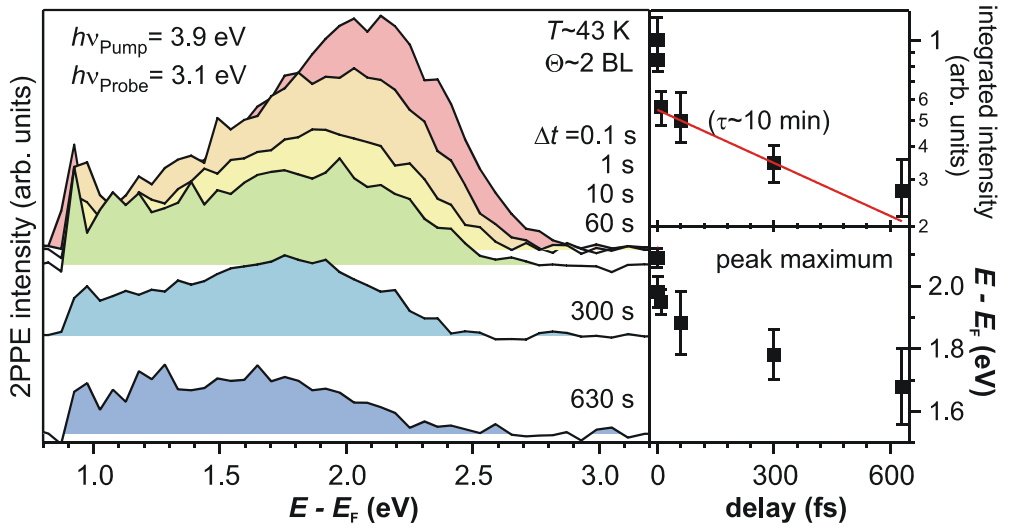

Fig. 2.11: *Ultralong-Living Electrons in Crystalline D_2O/Ru(001).* Left: 2PPE spectra at different time delays. Top: Integrated peak intensity as a function of time delay. Bottom: Transient shift of the peak maximum (adopted from [Gah04]).

even after minutes (bottom inset in Fig. 2.11). This observation indicates that the electron solvation (energetic stabilization) is not completed even in this late time regime.

It could be shown through a photon energy dependence of the e_T state that the excitation of this long-living state probably occurs via the image potential state of the D_2O/Ru(001) system. [Gah04, Bov07] This scenario corresponds to the injection mechanism of the solvated electrons in the amorphous adlayers, where the electrons are excited to the delocalized ice conduction band before localization in the ice layer (cf. 2.3.1).[9] The fundamental steps of charge injection, localization, and back transfer are depicted in Fig. 2.12. Metal electrons are excited and transferred to the delocalized image potential state at 3.15 eV above E_F (1). As they are detected at $E - E_F = 2.1$ eV after 0.1 s, they have to stabilize by more than one electron volt within this time (2). Being efficiently screened from the substrate, the back relaxation (3) occurs on much slower timescales than for the amorphous ice layers.

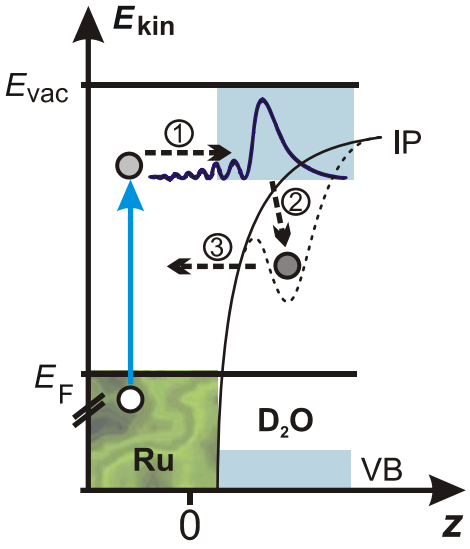

Fig. 2.12: *Process of Electron Trapping.* Excited metal electrons are transferred to the delocalized IPS (1), localize and stabilize (2). The back transfer to the metal (3) is very inefficient due to strong screening.

[9] In fact the image potential state can be set equal with the CB in crystalline ice. Due to the lack of long range order in the amorphous adlayers this feature broadens and appears as a continuum in the spectra.

Open Questions: No electron dynamics were observed on the ultrafast timescale. The injection via the IPS could only be indirectly deduced by a photon energy dependence. However, the solvated electron must exhibit formation dynamics. Paragraph 4.2.1 shows that this lack of dynamics on ultrafast timescales was due to the very low excitation and detection probability of the trapped electron. By improvement of statistics and data analysis, the ultraslow dynamics shown in Fig. 2.11 are completed in section 4.2 by the ultrafast *formation dynamics* of the trapped electrons.

The remarkable observation of electron stabilization occurring on minute timescales combined with a significant temperature dependence of the peak shift (see [Gah04] and 4.2.2) questions, which microscopic processes underlie these dynamics. A model calculation based on harmonic potentials is presented in 4.2.2, which explains the significant deceleration of the solvation dynamics by an overdamped harmonic oscillator with a temperature-dependent damping coefficient.

Summary

The preceding three sections gave an overview of the physics background of electron transfer and solvation phenomena in general and at interfaces in particular. It was shown that solvated electrons in front of metal surfaces are a model system for charge transfer processes, as they subsequently change their degree of confinement during solvation. For a comprehensive understanding of charge transfer both relevant coordinates, the electron *and* the solvent coordinate have to be considered. Yet, fruitful application of the respective approach to HET phenomena, Marcus or Landauer Theory, depends on the degree of electronic coupling to the substrate states. Furthermore, it was shown that for D_2O on metal surfaces the structure of the ice adlayer crucially determines the properties of the hydrated electron, their lifetime and energetic stabilization. However, detailed understanding of transfer and solvation phenomena at interfaces requires systematic investigation of the impact of substrate, adsorbate structure, solvation site, *and* employed solvent. In the present work electron transfer and solvation dynamics at the D_2O/Cu(111), D_2O/Ru(001), and the NH_3/Cu(111) interfaces are studied to gain such complementary insight into the underlying fundamental processes. As a basis, the next section discusses the elementary properties of all investigated adsorbates, substrates, and interfaces.

2.4 Ice- and Ammonia-Metal Interfaces

The study of electron transfer and solvation dynamics presented in this work was performed at solid ice- and ammonia-metal interfaces. The present section gives an overview of the physical properties of the adsorbates and substrates used in order to allow interpretation of the substrate, adsorbate, and structural influence on the electron dynamics at these interfaces.

2.4.1 Water-Ice and Ammonia

In this work, two different polar adsorbates, water-ice[10] and ammonia, were studied. Both molecules bind in their respective condensed phases via hydrogen (H-) bonds. These bonds form due to the electronegative character of the oxygen (nitrogen) atom. The hydrogen atom of the donating molecule remains covalently bound so that the H_2O (NH_3) remains intact. The distance between the hydrogen and the accepting oxygen (nitrogen) is considerably larger than the covalent bond length. This is why the H-bond is commonly termed O-H···O (N-H···N).

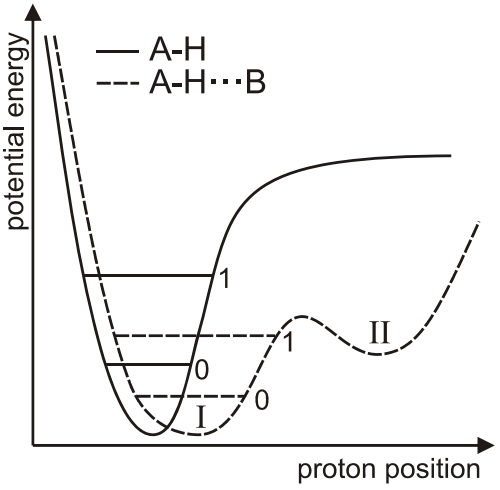

Fig. 2.13: *H-Bond and A-H-Group Potential.* The hydrogen bridge leads to the formation of a double potential. The vibrational modes shift due to the broadening of the potential minimum (based on [Nov74]).

Fig. 2.13 compares the potential of a bare A-H-group with a hydrogen-bonded one.[11] [Nov74] Due to the hydrogen bridge a second minimum forms. The H-bond potential is not symmetric, as the accepting oxygen atom is already covalently bound to two hydrogens. Additionally, the minima are broader in the H-bond case. This leads to a downward shift and a squeezing of the vibrational modes. Therefore, the O-H stretching mode is a measure for the binding strength of a hydrogen bridge. While the strength of the H-bonds in ice is ~240 meV, ammonia molecules bind considerably weaker with ~100 meV.

[10] If not stated otherwise, the terms "ice", "water", and "H_2O" represents both isotopes, H_2O and D_2O, in the following.
[11] A stands for an arbitrary hydrogen-bridged atom as e.g. oxygen in the case of water.

Water-Ice: Water is of general importance in a variety of different fields. It determines everyday life on a macroscopic scale, because it strongly influences the heat balance on the earth: 70% of the planet's surface area is covered by oceans and polar caps, which store energy and bind for example carbon dioxide. In addition, the high reflectivity of ice particles in the atmosphere contributes significantly to the terrestrial climate by e.g. the reflection of sunlight. But water also plays an important role on a microscopic scale: Biological cells consist of almost 100% water. As a solvent, it influences the charge transfer processes at membranes in biologic systems.

The water molecule, H_2O, has ten electrons, eight from the oxygen $(1s)^2(2s)^2(2p)^4$ and two from the covalently attached two hydrogen atoms, each with $(1s)^1$. As a first approximation, the binding may be described by a linear combination of these atomic orbitals: The (2s) and (2p) orbitals hybridize so that wave functions with tetrahedral symmetries result (sp^3-hybridization). These lead to the bent symmetry of the H_2O presented in Fig. 2.14a. Two electrons contribute to the bond with the hydrogen atoms. Both remaining electrons are in the highest occupied molecular orbitals (HOMO), and form the so-called lone pairs of the water molecule (Fig.2.14b). Because of the very high electron affinity of the oxygen atom, the orbitals of the oxygen atom are the ones predominantly filled with electrons; the protons cause only a very weak corrugation of the charge density distribution. Due to this effect and because of the negatively charged lone pairs, the water molecule exhibits a dipole moment of 1.85 D. The lowest unoccupied orbital (LUMO) of H_2O has – in contrast to the HOMO – a high residence probability at the protons and an anti-bonding character [Jor73].

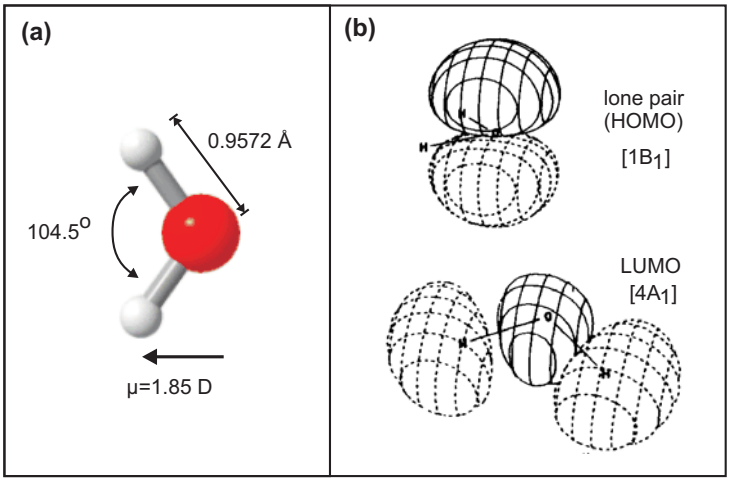

Fig. 2.14: *The Water Molecule and Its Orbitals.* (a) Geometry of a water molecule (based on [Lud01]). (b) Highest occupied and lowest unoccupied molecular orbitals (based on [Jor73]).

Under ambient conditions H_2O exists in three different phases, water vapor, liquid water, and ice. But in fact, the phase diagram of water is much more complicated. In addition to a variety of metastable phases, 13 stable crystalline phases are known [Pet99]. Most of them occur only under very high pressures on the order of several GPa. For the low pressure regime (ultrahigh vacuum (UHV)[12] up to ambient pressures) the phase diagram reduces to four stable and three metastable phases as depicted in Fig. 2.15.

[12] $p < 10^{-8}$ mbar

The measurements presented in this work were performed under UHV conditions and at sample temperatures above 20 K. In this pressure and temperature range only the three metastable structures of water shown in Fig. 2.15 occur. Amorphous solid water (ASW) forms at temperatures below 110 K. Around ~130 K a transition to a supercooled glass (*water A*) occurs before the ice crystallizes to the cubic ice I_c. Hexagonal ice I_h, commonly known as *crystalline ice,* cannot be reached under UHV conditions. Heating to 200 K would be required.

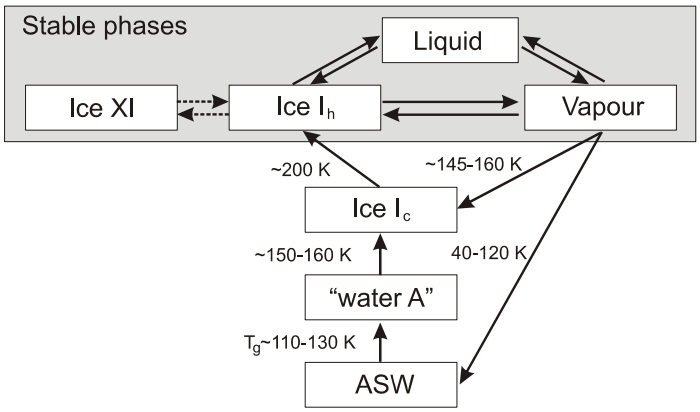

Fig. 2.15: *Simplified Phase Diagram of Water.* The stable and metastable phases of H_2O at low pressures (based on [Pet99].

As the onset of desorption for H_2O and D_2O lies at ~150 K, the $I_c \leftrightarrow I_h$ transition cannot be reached.[13] Only by adsorption of D_2O at 150 K and subsequent annealing to slightly higher temperatures can the transition to ice I_h, in principle, be achieved. The cubic ice differs from the hexagonal structure by the stacking order: While I_c is stacked in an ABABAB order, ice I_h is tiled up following an ABCABC arrangement.

The structure of ice I_h is stable under ambient pressures and known from many experiments. It consists of four-fold coordinated water molecules, all of them donating and accepting two H-bonds as depicted in Fig. 2.16a. The oxygen atoms are therefore ordered in a hexagonal lattice with a unit cell that consists of four molecules. At 100 K the lattice constants for H_2O (D_2O) are a = 4.4966 Å (4.4977 Å) and c = 7.3204 Å (7.3228 Å). [Röt94] However, the arrangement of hydrogen atoms within this oxygen network is not periodic. The so-called proton-disorder is not predictable. However, the alignment of the protons fulfills the Bernal-Fowler-Pauling ice rules within the hydrogen-bond network [Pau35, Ber33]:

(i) Each oxygen atom is covalently bound to two hydrogen atoms.

(ii) Exactly one hydrogen atom resides in between two neighboring oxygen atoms.

Fig. 2.16b presents a top and a side view of the structure of ice I_h. It is arranged in so-called ice bilayers (BL): Three molecules of the hexagons (darker molecules in Fig. 2.16b, top) lie 0.9 Å higher than the other two, which leads to a buckling in the hydrogen-bonded network. The grey shaded area indicates the top view of the unit cell. The bottom part of Fig. 2.16b depicts the side view of crystalline ice. The dark molecules belong to the unit cell. The concept of the ice bilayer is used later for the quantification of D_2O coverage on metal surfaces; a detailed description of this approach is given in the subsections 2.4.3 and 3.3.2.

[13] A detailed description of the preparation conditions and thermal desorption spectra are given in subsection 3.3.2.

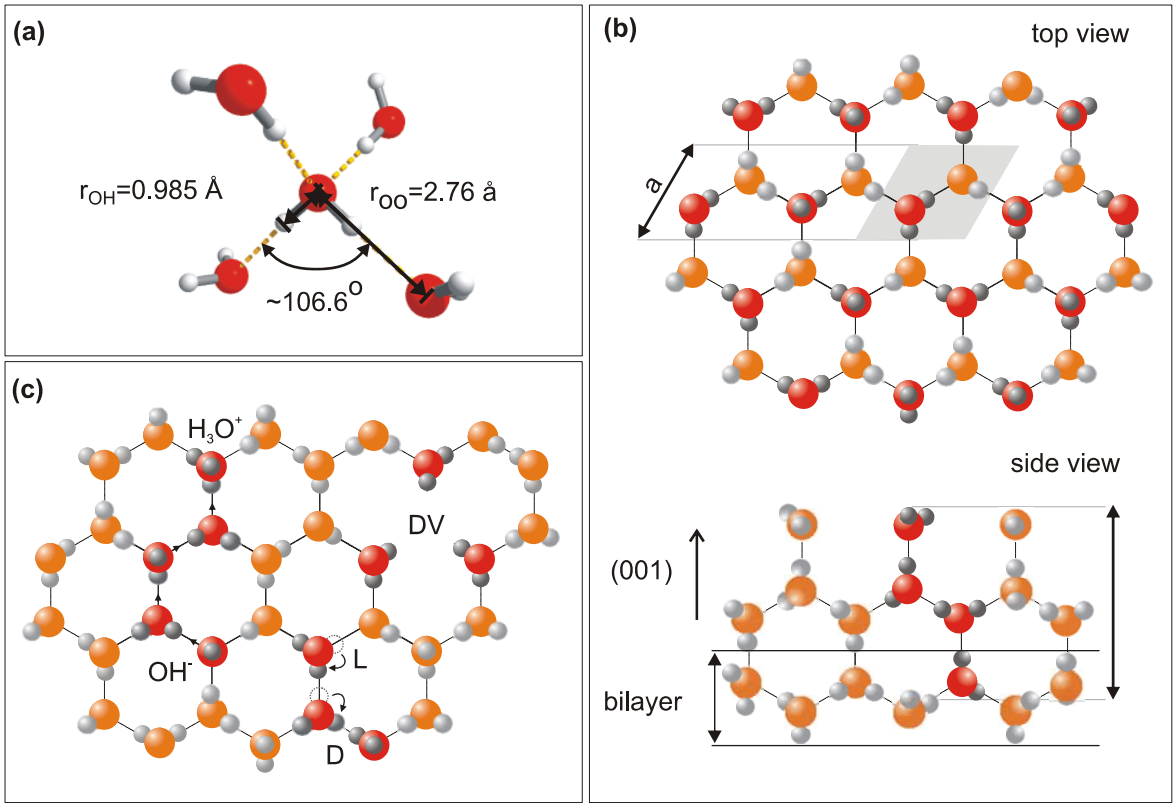

Fig. 2.16: *Structure of Ice I_h and Point Defects.* (a) Four-fold coordination of H_2O molecules within the lattice (based on [Lud01]). (b) Top and side view of one (two) ice bilayers The unit cell is indicated by the gray shaded area (top view) and the darker molecules (side view). The proton disorder becomes apparent. (c) Ionic and Bjerrum defects in ice I_h. The DV defect is a combination of a vacancy with a D-defect (see text for details).

Point defects in a perfect crystalline structure play an important role for the properties of ice. For example, the transition from one ice configuration to another is mediated by defects. The proton-ordered phase ice XI mentioned in Fig. 2.15 can only be reached at temperatures below 76 K and with the addition of defects to ice I_h, as the natural defect density in ice I_h is not sufficient to establish proton order within finite timescales [Joh98]. Also the electric conductivity and dielectric relaxation in the presence on an electric field are strongly related to the defect density in crystalline ice [Pet99]. However, defects in the structure of the investigated ice adlayers are promising candidates for electron traps, because they disturb the periodicity of the lattice and hence cause fluctuations of the potential energy surface.

The protonic point defects of ice I_h are shown in Fig. 2.16c. In all cases one of the ice rules is violated, but the hexagonal lattice of the oxygen atoms remains. In principle the point defects can be separated into two main categories: (i) Ionic and (ii) Bjerrum defects.

(i) Ionic defects occur by a violation the first ice rule: A proton transfers from one water molecule to the neighboring one. As this situation is energetically unfavorable (cf. Fig. 2.13), the next molecule will hand over another proton to its respective neighbor. This subsequent separation of the H_3O^+ and the OH^- ion is depicted in

Fig. 2.16c (left). The protons tunnel within the existing double minimum H-bond potential from lattice site to lattice site.[14]

(ii) Bjerrum defects [Bje52] occur if the second ice rule is violated, i.e. one O-O axis exhibits either two hydrogens (D-defect) or no (L-defect) proton (Fig. 2.16c, bottom). The energy cost for formation of these defect pairs is only half as high as the one for the ionic defects.[15]

The protonic conductivity of ice depends strongly on the defect density and the ratio between ionic and Bjerrum defects. The latter is important, because it is impossible that the same kind of defect travels along the same path right after the other; ionic and Bjerrum defects have to alternate. Therefore, the elementary charge e is divided between the two: Ionic defects carry an effective charge of $\pm 0.62e$, the Bjerrum defects of $\pm 0.38e$. However, the defect concentration is with 10^{-13} in ice at -20°, very low (liquid water has pH = 7), so that its intrinsic conductivity is negligible. It is assumed that the observed conductivity of crystalline ice results from impurities. [Pet83]

The second investigated ice structure occurring under UHV conditions is amorphous solid water.[16] Its main characteristic is its lack of long range order, although the local structure is very similar to ice I_h: From X-ray and neutron diffraction experiments it is known that each water molecule is surrounded by 3.9(1) neighboring molecules. [Sce82, Fin02] Due to deviations of 8° (on average) from the tetrahedral angle the structural correlation is already lost after 7 Å. The differences of crystalline and amorphous structures are sketched in Fig. 2.17 (left).

The morphology of amorphous ice is strongly influenced by the respective preparation conditions. For temperatures below 90 K, pores form in the ice, depending on velocity and direction of the incoming molecules. [Ste99, Azr99] At higher preparation temperatures and employing a molecular beam aligned perpendicularly to the surface, smooth amorphous layers form (see also subsections 2.4.3 and 3.3.2).

Fig. 2.17 illustrates the differences between a crystalline and an amorphous solid. This distinction is important for the present work, as the electron solvation dynamics in amorphous *and* crystalline adlayers are investigated here. Deviations from the periodic structure in the lattice of an amorphous solid discussed above cause differences in the electronic band structure and Brioullin Zone. This effect becomes apparent in the right panel of Fig. 2.17. All sharp features in the density of states (DOS) of the crystalline solid (top), which originate from the periodicity of its lattice, become smooth for the amorphous structure. Besides sub-structures in the valence band (VB) and conduction band (CB) also the band edges are washed out and

[14] The activation energy of this motion is close to zero, so that a rather high mobility of these defects on the order of 10^{-7} m^2/Vs results. On the other hand, the initial activation of the ionic pair formation is, with ~1.4 eV, very high. [Pet99]

[15] The mobility of L-defects is, with $2 \cdot 10^{-8}$ m^2/Vs, one order of magnitude smaller than for the ionic defects, which is correlated with the higher activation energy of motion of 200-300 meV. At first sight, it is puzzling that no mobility of D-defects has been measured yet, as the involved processes (reorientation of H_2O molecules) are similar for both, the D- and L-defect motion. A possible reason for this discrepancy is the trapping of D-defects at vacancies in the ice lattice as shown in Fig. 2.16c (right). [Pet99]

[16] As no other amorphous phase of ice than ASW is discussed in this work, it is simply termed amorphous ice.

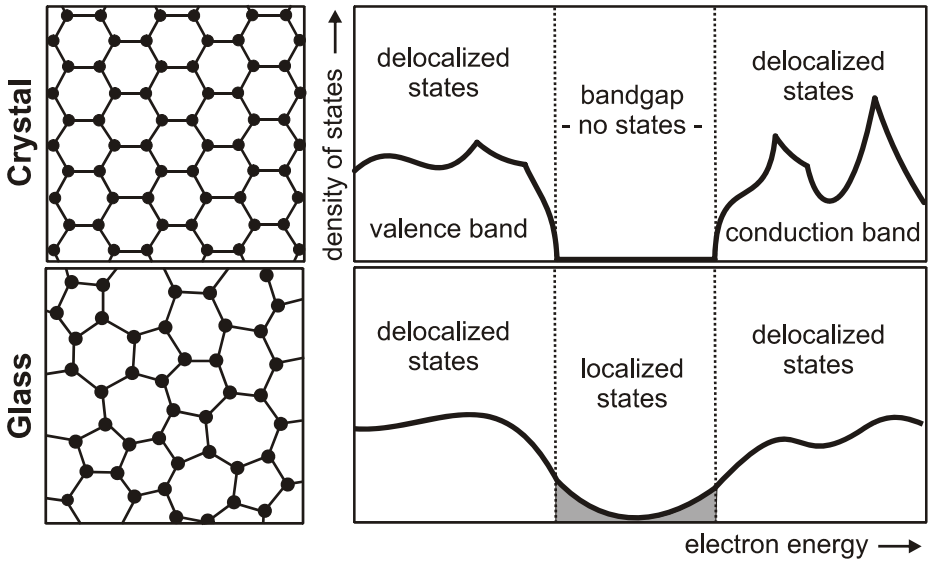

Fig. 2.17: *Comparison of a Crystalline and an Amorphous Solid.* Left: Schematic representation of the similar local structure and the missing long-range order of an amorphous solid. Right: Schematic density of states of a crystalline and an amophous solid. The sharp features of the periodic lattice are washed out by the lattice distortions in the glassy structure (based on [Zal83]).

decay exponentially into the band gap [Gou90]. These states below the CB minimum and the VB maximum, contrary to the electronic states in delocalized bands[17], result from localized states in the solid. Localized states occur if they are more stable than the delocalized ones, i.e. the potential energy gain has to be higher than the loss of kinetic energy resulting from the localization according to Heisenberg's Uncertainty Principle. This so-called *Anderson-Localization* is also observed for the solvated electrons in D_2O/Cu(111) discussed in 2.3.1: The solvated electron state e_S lies near the conduction band minimum in Fig. 2.09.

Ammonia: The ammonia (NH_3) molecule has – as water – ten electrons, in the configurations $(1s)^2$ $(2s)^2$ $(2p)^3$ of the nitrogen and $(1s)^1$ for the three hydrogen atoms. The bonding results from an sp^3-hybridization of the 2s and 2p electrons; three of the tetrahedrally arranged sp^3 orbitals contribute to the bonds with the hydrogens. Two nitrogen electrons reside in the fourth hybrid orbital leading to an H-N-H angle of 107° (cf. Fig. 2.18a). The far field resulting from the electron distribution is like the one of water a dipole field with a slightly smaller dipole moment of 1.47 D.

As water, ammonia forms hydrogen bonds in its liquid and solid phases. However, as NH_3 only offers one lone pair, but three hydrogen atoms, it is not possible to "saturate" all protons in H-bonds. In addition the binding strength of an ammonia H-bond is, with 0.1 eV, much weaker than the 0.24 eV of ice.

[17] The spatial extension of CB electrons is due to the proton disorder and defects, which is considerably smaller than in metals. For liquid water the radius is however >30 Å [Kee01].

Compared with water, very little is known about the phase diagram of ammonia. Besides some high pressure and temperature phases, which are not discussed here, NH_3 exhibits a crystalline phase for T < ~210 K and pressures below ~ 1GPa. [Gau88] Its structure is shown in Fig. 2.18b. In contrast to ice, the H-bonds are not straight, but have an angle of 160°. The N-H···N length is with more than 3 Å larger than in ice I_h. For adlayers under UHV conditions metastable, amorphous structures of ammonia have also been found on metal surfaces (cf. 2.4.3).

Liquid ammonia exhibits one extraordinary characteristic when considerably doped with alkali metal atoms: For concentrations higher than ~8 mol% the solution becomes *metallic* and is therefore termed *liquid metal*. [Tho76] Already 100 years ago, Kraus found that the metal valence electron was surrounded "by an envelope of solvent molecules" in dilute solutions, but was free in concentrated ones. [Kra08] He concluded that the high mobility of these electrons contributes to the high conductivity (> 10^4 $\Omega^{-1}cm^{-1}$) of the solution.[18] This conclusion is noteworthy, because the Drude Model for metals was proposed only eight years earlier, in the year 1900. Since then, much effort was put into the investigation of the metal-nonmetal transition. [19] One possible explanation for the transition was provided by Mott and Davis, who argued that as soon as the density of states becomes too low in a non-crystalline material, the states become localized. This localization can occur close to band edges and in the so-called *pseudogap* between bands. [Mot71] The Coulomb interaction between the metal valence electrons leads to the localization and solvation at low concentrations. For higher densities the interparticle distance is reduced, so that the screening effectively decreases. The electrons are free, experience a well-defined low-range order due to the solvated ions, and the solution becomes metallic. Cohen and Jortner in contrast proposed a percolation model in which large scale fluctuations lead to localization of the charge carriers. [Coh73] This may be understood by density fluctuations in the liquid; electrons localize in the dilute region, because a transfer from one electrode to the other via "hopping" between metallic (dense) patches becomes improbable. [Tho76]

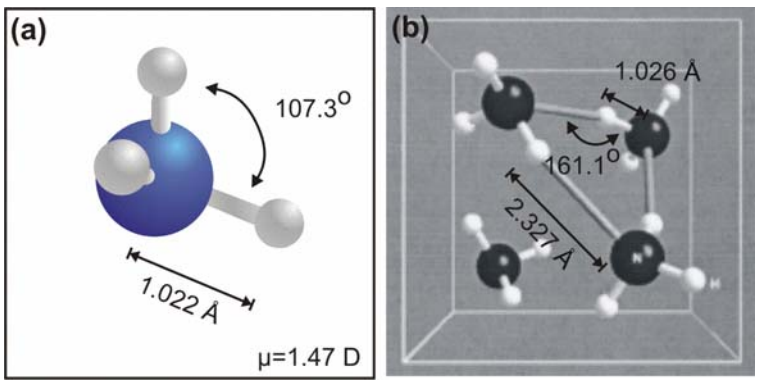

Fig. 2.18: *Ammonia.* (a) Geometry of the ammonia molecule. (b) Hydrogen bonding in crystalline ammonia I (adopted from [For03]).

[18] The conductivity of iron is 10^4 $\Omega^{-1}cm^{-1}$ at 295 K. [Kit99]

[19] Such transitions are also often termed metal-to-insulator transitions. However, most publications about the transition of liquid ammonia use the term metal-nonmetal transition.

Today, studies still focus on the metal-nonmetal transition of alkalis solvated in ammonia. [Hay02, Tho03, Was03, Tho04] The main goal of these works is to gain deeper insight into the structure of the ammonia solutions by the detailed investigation of the solvent-ion, solvent-electron, ion-ion, ion-electron, and electron-electron interactions. It is concluded that the electrons are trapped in Bjerrum-type (see Fig. 2.16c) polaronic cavities formed by "free" solvent molecules.[20] [Hay02] The authors also state that – due to volume estimates – a spin-paired species, i.e. electron solvation of *two* charges within one shell, is predominant. In [Was03] it is shown that the excess electron is completely dissociated from the parent ion, supporting Mott's suggestion of a metal-nonmetal transition due to Coulomb interaction. At saturation with lithium, every ammonia molecule is partly incorporated into an ion solvation shell, so that electrons cannot be trapped anymore. [Tho04]

In this work no alkali metal solvation is performed. Doping the ammonia with 8 mol% of metal atoms (and therefore 8 mol% of electrons) would correspond to an excitation of 16 mol% of excess electrons in the ammonia adlayer. Such a high excitation of the more than 10^{15} molecules per cm^2 is impossible to achieve with the employed UV fluences of ~0.02 mJ/cm^2 ($4 \cdot 10^{13}$ photons per pulse and cm^2 for $h\nu = 3$ eV).

2.4.2 Electronic Properties of Cu(111) and Ru(001)

The substrate used plays – in addition to the properties of the adsorbate – an important role in the time-resolved 2PPE measurements. On the one hand it serves as a template for the adlayers and therefore influences the adsorbate structure (cf. 2.4.3). But as interfacial electronic states may overlap with states in the metal, their dynamics and energetics are strongly influenced by the respective substrate. Depending on the adsorbate structure and its interaction with the substrate, also bare metal features may occur in the spectra. Thus, a description of the two employed templates and their electronic surface band structures is given in the following two sections.

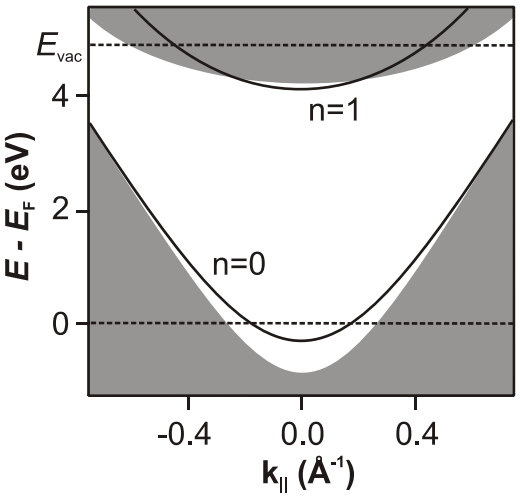

Fig. 2.19: *Projected Surface Band Structure of Cu(111).* The sp-band exhibits an orientation-al bandgap around $k_{||} = 0$ (based on [Smi85]).

The Cu(111) Surface: Because bulk copper grows as an fcc (*face-centered cubic*) single crystal, its (111)-surface is hexagonal.[21] The rather simple projected surface electronic band structure (nearly free electron-like) has made Cu(111) one of the most investigated single crystal surfaces for electron dynamics [Pet98, Kno98, Bür99, Kli00,

[20] An ammonia molecule is considered to be "free" if it does not contribute to the solvation of another electron or alkali ion.
[21] Lattice constant: 2.5561 Å [Kit99]

Rei00]: The d-bands of Cu[22] lie 5-2 eV below the Fermi Level E_F and are therefore completely occupied. In contrast, the sp-band of the 4s and 4p states ranges from 8.6 eV below E_F and up to states above the vacuum level E_{vac}. Fig 2.19 presents the projected surface band structure of Cu(111), which shows its orientational sp-band gap around the center of the surface Brioullin zone. Due to this gap surface states and also adsorbate-induced spectral features can only exhibit wave functions that are exponentially damped inside the bulk; the penetration depth of such states strongly depends on their energy separation from the gap edges [Smi85]. The work function Φ, i.e. the difference between Fermi and vacuum level, is for Cu(111) 4.94(5) eV. [Fau95, Kno97a]

The electronic band structure of a metal results from its periodic lattice that extends in all dimensions to infinity. The band gap originates from Bragg Reflection of the electronic wave functions at the Brioullin Zone boundaries. At a surface the infinite periodicity is broken in one direction. Due to this symmetry loss, new states can form within the band gap, the so-called surface states. In a nearly-free electron metal as copper, these states are delocalized parallel to the surface and termed Shockley surface states.[23] [Zan88] At the Cu(111) surface this two-dimensional, delocalized state is partially occupied, because it lies at the center of the Brillouin zone ($k_{\parallel} = 0$) 0.4 eV below the Fermi Level (cf. Fig. 2.19). The $n = 0$ surface state of Cu(111) can therefore serve as a very efficient source for the excitation of electrons into other states at the interface. [Hot99] The unoccupied parts of the Shockley band, in contrast, offer a large phase space for scattering processes. The lifetime of the first image potential state of Cu(111) (see further below), for example, results to 40% from this decay channel. [Osm99].

An electron in front of a metal surface induces a charge density at the sample-vacuum interface that screens it from the metal. The resulting potential is similar to the classical potential of an image charge with the distance $2z$ (see Fig. 2.20a): [24]

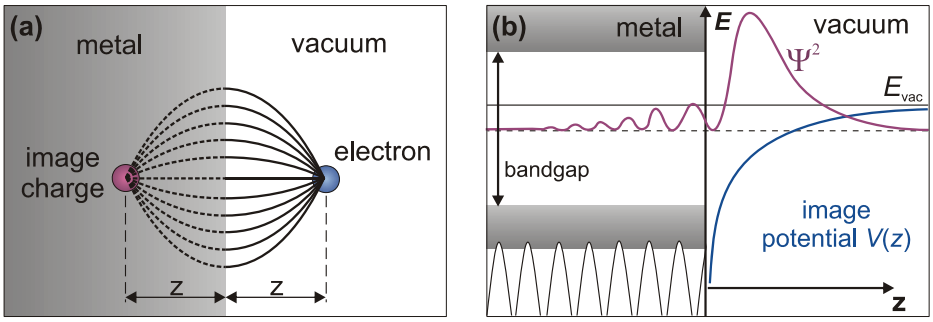

Fig. 2.20: *Image Potential State.* (a) An electron induces a polarization in the metal. (b) The resulting image potential gives rise to two-dimensional, bound states that are damped exponentially inside metals exhibiting a bandgap.

[22] Electron configuration: (Ar) $(3d)^{10}(4s)^1$

[23] In the case of a strong potential perturbation at the surface localized so-called Tamm states occur. They can be theoretically explained by the tight-binding approach and are, for example, found at semiconductor surfaces were a covalent bond is broken at the surface. [Zan88]

$$V_{IP} = \frac{1}{2} \cdot \frac{e^2}{2(z - z_0)} \tag{2.6}$$

z_0 denotes the mirror plain, which lies approximately half a layer distance outside the last atomic layer. [Smi89] The states arising from this potential are, because of the two dimensional periodicity of the interfacial plane, delocalized parallel to the surface. Due to the similarities with the electrostatic problem of a point charge, they are termed image potential states (IPS). If the metal exhibits a band gap, the electronic wave function decays exponentially into the metal (Fig. 2.20b) and a Rydberg-like series of states evolves at the interface:

$$E_n = E_{vac} - \frac{1\mathrm{Ry}}{4(n+a)^2} \quad \text{with} \quad n = 1, 2, 3, \ldots \tag{2.7}$$

Here, n is the quantum number, denoting the number of nodes in front of the metal surface, and a is the quantum defect that accounts for the finite penetration depth of the wave function into the metal. This occurs, because the metal does not present an infinitely high potential barrier.

The n = 1 IPS of the Cu(111) surface lies around $k_\parallel$ = 0 within the sp-band gap (see Fig. 2.19) and has a rather short lifetime of ~20 fs. [Kno97a, Ech04] This is due to its proximity to the band gap edge: The wave function decays slowly into the metal. [Wei02] The n = 2 lies above the band gap and is therefore degenerate with bulk metal states, which leads to a reduction of its lifetime to 14(3) fs [Ech04] compared with the n = 1. The surface and the image potential states of the Cu(111) surface have been investigated extensively during the last years [Kno97a, Bür00, Rei01, Kli00] and are also very well understood theoretically [Ech00, Ech04].

The Ru(001) Surface: Because bulk ruthenium is an hcp (*hexagonal closed packed*) single crystal, its (001) surface is, as the Cu(111) surface, hexagonal.[25,26] The electronic bandstructure of the Ru(001) surface is dominated by the partially unoccupied d-bands of the transition metal ruthenium[27]. They lead – as depicted in Fig. 2.21 – to a considerable maximum of the DOS 1 eV above the Fermi Level. At the (001) surface these d-bands lead to a surface resonance, which lies slightly below 1 eV. [Sei00] The resulting large phase space for scattering processes leads to four times shorter relaxation times of excited electronic states than for Cu(111). [Kno98, Lis04, Lis05]

Ru(001) exhibits an orientational sp-band gap, which ranges – in contrast to Cu(111) – from 1.6 eV to 11 eV *above* the Fermi Level. Therefore, it is within the energy range of unoccupied,

[24] In atomic units, i.e. $\hbar = m_e = c = 1$.
[25] In literature this surface is also termed Ru(0001). This notation originates from crystallography and is used for hexagonal surfaces only. The first number is a linear combination of the following two, so that a third zero results in the present case.
[26] Lattice constant: 2.7059 Å [Kit99]
[27] Electron configuration: (Kr) $(4d)^7$ $(5s)^1$

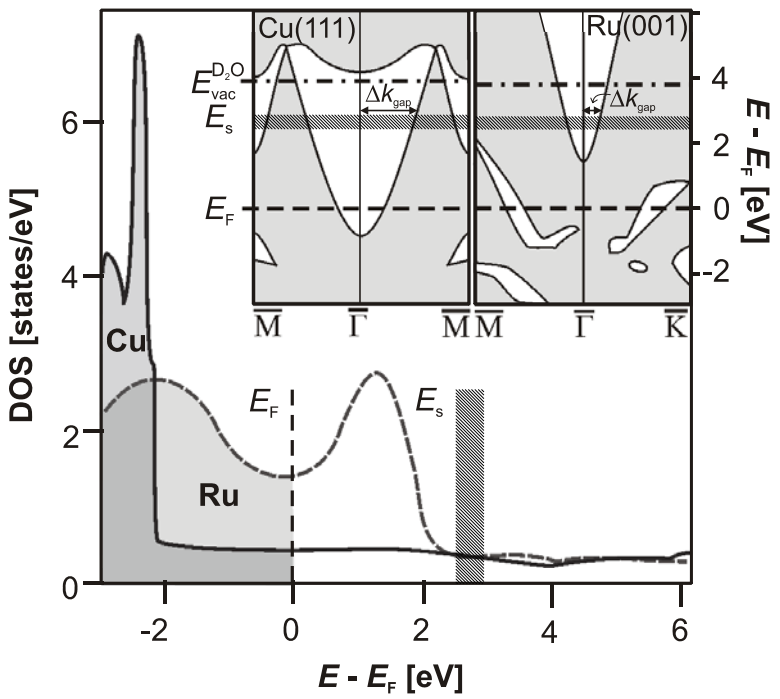

Fig. 2.21: *Electronic Surface Bandstructures and Densities of States of the Investigated Substrates.* Main Figure: The DOS of Ru exhibits a maximum 1 eV above the Fermi Level due to its unoccupied d-bands. The DOS of Cu is relatively flat. (DOS redrawn from [Pap86].) Inset: Both substrates have an orientational sp-band gap. For Ru(001) it lies higher in energy so that its width Δk_{gap} is narrower in k-space. E_s denotes the energy at which solvated electrons occur in ice layers on the respective substrates. The influence of the substrates electronic properties on the electron dynamics is discussed in 4.1.1. (Band structures redrawn from [Sei00, Zan88]

bound states between E_F and E_{vac}[28] considerably narrower in k-space than the one of Cu(111). This may have impact on the decay probability of excited electrons by elastic scattering as mentioned before in paragraph 2.1.1.

As the band gap of the Ru(001) extends across E_{vac}, a full series of IPS forms that is *not* degenerate with metal states at $k_{\parallel} = 0$ (as in the case of the $n = 2$ for Cu(111)). Their dynamics were investigated within the framework of Cornelius Gahl's dissertation. [Gah04] The results are given in Tab. 2.01. It is obvious that the lifetime of the IPS increases with increasing quantum number. This is due to the fact that with a rising number of nodes of the interfacial wave function the maximum charge density has a larger distance to the interface. This decreases the wave function overlap with the metal and therefore the decay probability.

n	binding energy (eV)	lifetime (fs)	line width (meV)
1	-0.661(20)	11(2)	61(5)
2	-0.187(15)	57(5)	22(4)
3	-0.087(10)	174(10)	-
4	(-0.050)	(413(35))	-
5	(-0.032)	(791(60))	-
6	(-0.023)	-	-
7	(-0.017)	-	-

Tab. 2.01: *Image Potential States on the Bare Ru(001) Surface* (adopted from [Gah04]).

2.4.3 D_2O and NH_3 on Metal Surfaces

Having discussed the properties of the investigated adsorbates and substrates, this section summarizes ice and ammonia adsorption on metal surfaces. While ice layers on metal (and semiconductor) surfaces of various structures and thicknesses have been the subject of many investigations in the past decades, [Hel94, Smi96, Ste99, Fei02, Hen02, Bov03, Mic03, Den03, Men05, Zha06a] the structure and electron dynamics at ammonia-metal interfaces have hardly been studied.

Ice on Metal Surfaces: The ice bilayer (BL) is used as a mass equivalent for the ice coverage on a substrate and is attributed to one double layer in crystalline ice I_h, as introduced in Fig. 2.16b. Yet, due to the ice-metal interaction, the *adsorbed* ice bilayer must not necessarily have the same structure as the *bulk* ice bilayer.[29] Because of the strong Ru-water interaction, for example, it is generally accepted that the first D_2O BL wets the Ru(001) surface.[30] For Cu(111) it is known, however, that the first three BL adsorb in clusters before layerwise growth. [Gah03, Meh05] In both cases the lone pairs of every second water molecule bind to substrate atoms and their protons form H-bonds with the second half bilayer (Fig. 2.22a). The charge transfer from the molecules to the substrate and the dipole moment, which is induced by the orientation of the D_2O, lead to a lowering of the sample work function by ~1 eV (see chapter 4 and [Gah04]).

Despite the numerous publications, the structure of the first bilayer of D_2O on the Ru(001) surface is still under discussion. [Hel94, Hel95a, Hel95b, Fei02, Den03 Fei03, Pui03, Mic03, And04, Fei04, Men05] The debate began when Held and Menzel showed, using low energy electron diffraction (LEED) measurements, that the vertical distance between oxygen atoms in the two halves of the first bilayer on Ru(001) adds up to only 0.1 Å. [Hel94] This considerable deviation from the "bulk bilayer" (~0.9 Å, Fig. 2.22a) could not be explained either by the expansion of the layer due to the lattice mismatch or by the slight surface reconstruction of Ru(001). [Hel94, Pui03] Since positions of the deuterium atoms cannot be determined by LEED, various speculations of their arrangement arose. Feibelman suggested, on the basis of density functional theory (DFT) calculations, that a half-dissociated structure is the most stable one on Ru(001). [Fei02] As sketched in Fig. 2.22b, half of the water molecules dissociate so that a deuterium atom is bound in the middle of every ice hexagon, and one D_2O is exchanged by an OD. While the oxygen positions are quite well reproduced, the work function decrease of 0.3 eV is much too low; adsorption of 1 BL D_2O on Ru(001) leads to a lowering of the work function by 1.2 eV. [Hel95a, Gah04]

---

[28] The work function of bare Ru(001) is 5.4 eV. [Ber00]

[29] Most investigations on adsorbed ice layers were done on hexagonal surfaces, as symmetry and structure fit best here. [Thi87, Hen02]

[30] Ice adsorption on Ru(001) is governed by a strong isotope effect: H_2O adsorbs in contrast to D_2O in stripes on the ruthenium surface, which is generally explained by the considerably different zero-point energies of the isotopes (*Ubelohde Effect*). [Hel95a]

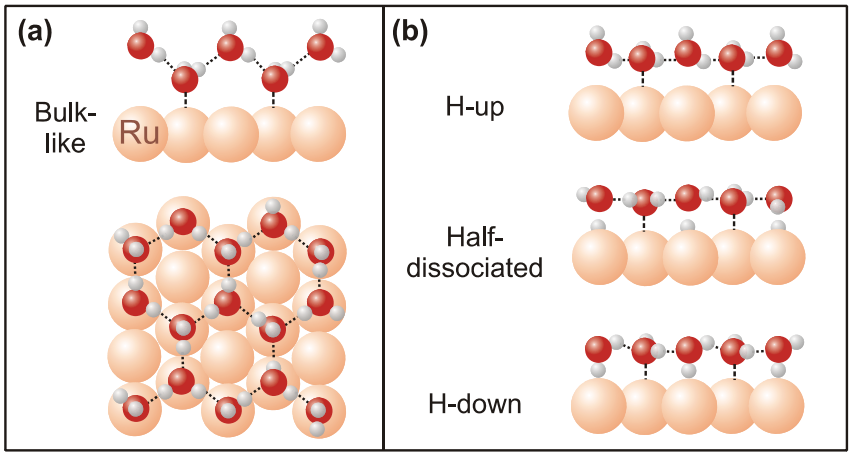

Fig. 2.22: *The Water Bilayer on Ru(001).* (a) Arrangement of D_2O molecules on the Ru(001) surface according to the bulk-like ice bilayer. (b) Alternative adsorption scenarios explaning the small O-O distance.

Sum-frequency generation (SFG) studies of the system confirm the absence of the O-D-stretch vibration, but do not reproduce all features predicted by the DFT calculations. [Den03, Fei03, Fei04] As an alternative the H-down structure of Fig.2.22b is suggested, because it also successfully explains the lack of O-D vibrations. However, DFT calculations of this structure also do not reproduce the measured work function change (cf. Tab. 2.02).

Recent *ab initio* molecular dynamics calculations show that the D-up and D-down structure are energetically degenerate and that the half-dissociated structure is indeed energetically more stable (ΔE = 0.24 eV). But as the calculated dissociation barrier is, with 0.62 eV, higher than the adsorption energy of the molecular bilayer (0.53 eV), the half-dissociated structure can be excluded for low temperatures. [Men05] Instead, the authors suggest a mixed D-up and D-down structure, which could explain the strong work function change upon bilayer adsorption (cf. Table 2.02). In addition, Faradzhev et al. could show that the cross section for electron-induced dissociation of D_2O/Ru(001) is very high for low energy electrons. They suggest that the bilayers investigated by Held and Menzel in 1994 by LEED were indeed partially dissociated, but not because of preferable adsorption of this structure: The bombardment with electrons dissociated the ice. [Far05] Appendix B presents work function measurements of the first bilayer on Ru(001) as a function of electron exposure. Later, it is shown that the work function rises upon elecron bombardment, supporting the above scenario.

D_2O adsorption on Cu(111) differs significantly from that on Ru(001). Due to a much weaker ice-metal interaction the first layers of water do not wet the surface. The ice-ice interaction is of comparable strength to the ice-metal interaction, so that adsorption occurs in clusters for coverages below 3 BL. STM (*scanning tunneling microscopy*) images of these structures are presented in paragraph 4.1.2.

Structure	D-up	1:1	1:2	1:3	D-down	Half-diss.	Exp.
$\Delta\Phi$ (eV)	3.01	1.70	1.54	0.82	0.40	0.34	1.26

Tab. 2.02: *Work Function Change for Different Bilayer Structures (adopted from [Men05]).*

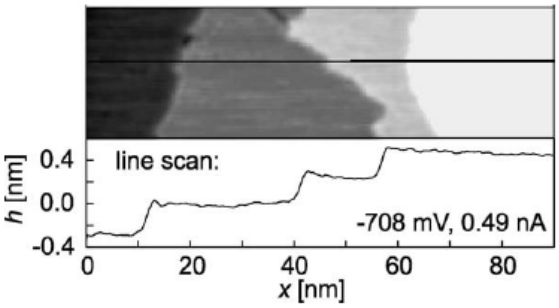

Fig. 2.23: *STM Image of an H_2O Multilayer on Cu(111).* The line scan illustrates the steps of the height of one H_2O bilayer (adopted from [Gah03]).

Above 3 BL, smooth, amorphous ice layers grow on the Cu(111) template for temperatures below 110 K as depicted in Fig. 2.23 for H_2O/Cu(111). [Gah03] For Ru(001), where the first D_2O bilayer already wets the metal surface, it is assumed that for higher coverages the water adsorbs in smooth, amorphous layers, too.

It was shown previously for the D_2O/Pt(111) system that the morphology of amorphous ice layers on metal surfaces depends strongly on the preparation conditions. [Ste99] The temperature of the sample, the velocity, and the angle of incidence of the molecular beam can lead to highly porous adlayers. Collaborating with Morgenstern and Mehlhorn, a temperature dependence of the ice cluster morphology for the D_2O/Cu(111) system was found. [Meh05, Stä07] The results of this study, including the impact of the cluster structure on the electron dynamics, are presented in section 4.1.2 and 4.1.3.

As discussed above, D_2O crystallizes under UHV conditions between 150 and 160 K. However, in how far this transition from the metastable amorphous structure to the crystalline phase is governed by island formation of the multilayer coverages on the Cu(111) and Ru(001) substrates is still unknown. However, recent STM studies on the crystallization of D_2O *clusters* on the Cu(111) surface [Meh05] show that the amorphous islands shrink in width and increase in height upon crystallization. The impact of this structural transition on the electron transfer and solvation dynamics is discussed in paragraph 4.1.3.

Ammonia on Metal Surfaces: NH_3 binds on Cu(111) with its nitrogen lone pair on the atop site of the copper surface atoms (cf. Fig. 2.24) as shown experimentally [Bau00] and theoretically [Rob02]. The hydrogen atoms are oriented to the bridge sites of the Cu(111) surface. The DFT calculations also found a lifting (0.2 Å) of the underlying copper atom by the NH_3 adsorption, [Rob02] which could not be reproduced by photoelectron diffraction measurements due to a lack of sensitivity (-0.06 ± 0.4 Å, [Bau00]).

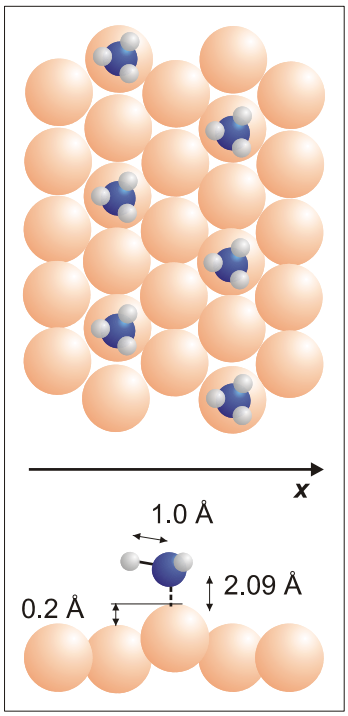

Fig. 2.24: *Monolayer Adsorption of NH_3 on Cu(111).* The nitrogen atom binds on the atop site of the copper atoms (numbers adopted from [Bau00, Rob02]).

From thermal desorption (TD) experiments it is known that the second monolayer is more strongly bound than the following (multi-) layers. [Her95] A detailed discussion of this work is given in section 3.3.2.[31] However, the authors find a strong change of the work function (-3.0 eV) upon ammonia multilayer adsorption. Similar behavior was also found for NH_3/Pt(111). [Fis81] This strong change is explained by the charge transfer from the molecule into the substrate and by a large dipole moment induced due to the orientation of the ammonia molecules along the surface normal. It is assumed that the ammonia multilayer forms an amorphous structure for the first two monolayers of NH_3/Ru(001). It is shown by TD experiments in paragraph 3.3.2, that a structural transition occurs for NH_3/Cu(111) at 100 K, which is assigned to the crystallization of the adlayer. As discussed in chapter 5, this transition is also governed by a change of electron dynamics.

Having introduced the fundamental processes of electron transfer and solvation at interfaces and having described the adsorbates and substrates investigated, the next chapter gives an overview of the experimental details, the technique, setup, sample preparation, and data analysis. In particular the sections 3.3 and 3.4 serve as a basis for the subsequent result chapters, as reliable data analysis and the knowledge of the adsorbate structure and coverage is crucial for the interpretation of the results.

[31] Note that different notations exist for the absolute coverage of ammonia on metal surfaces: Often the relative number of NH_3 molecules compared to underlying Cu atoms in the unit cell is used, for example Θ(monolayer) = 0.25. In the present work this monolayer coverage is used as a mass equivalent to have a more demonstrative measure for the coverage (consistent with the D_2O/metal notation, where 1 BL is the mass equivalent).